Shallow seismic investigations of the accretionary complex offshore Central Chile

Sebastián Obando-Orrego[1], Eduardo Contreras-Reyes[1], Anne M. Tréhu[2], and Joerg Bialas[3]

[1] Departamento de Geofísica, Facultad de Ciencias Físicas y Matemáticas, Universidad de Chile, Santiago, Chile.

[2] College of Earth, Ocean and Atmospheric Sciences, Oregon State University, Corvallis, Oregon 97331-5503, USA.

[3] GEOMAR Helmholtz Centre for Ocean Research Kiel, Division of Marine Geodynamics, Kiel, Germany.

Abstract

Thrust ridges are accretionary structures often associated with local uplift along splay faults and cold seep activity. We study the influence of a NS-trending thrust ridge system on the transition between the accretionary prism and the continental framework (shelf break) offshore the Maule Region (central Chile at 35º-36ºS) by examining its 2-D and 3-D seismic velocity structure. The experiment comprises five densely spaced seismic refraction lines running subparallel to the trench and recorded at nine OBH/S (ocean bottom hydrophone/seismometers) deployed along the central line. Results show a narrow margin-parallel volume (approximately 6x50x5 km^3) whose velocity distribution is consistent with sedimentary rocks. The shallow sedimentary unit is characterized by the presence of very low velocity hydrate-bearing sediments (<1.7 km/s), which are interpreted as highly porous sedimentary rocks (> 50% porosity) within the Gas Hydrate Stability Zone (GHSZ) suggesting low hydrate content. These zones spatially correlate with fluid activity in the vicinity of the NS trending thrust ridges based on local high heat flow values (>40 mWm^{-2}) and seepage mapping. On the other

hand, the splay faults that crop out on the flanks of the thrust ridge structures might be responsible for tectonically induced vertical fluid migration.

Key Words: Accretionary Prism; fluid migration; Chile; splay fault; sediment

1. Introduction

Accretionary convergent margins are typically characterized by a slow convergence rate (<7.6 cm/year) and trench sediment thickness greater than 1 km (Clift and Vannucchi, 2004). This is the case of the Nankai (Moore et al., 1990), Cascadia (Hyndman et al., 2011), and south-central (SC) Chile (Contreras-Reyes et al, 2010) margins. Trench sediments can be accreted frontally (forming a large accretionary prism with low slope angle), or basally (causing oversteepening of the continental slope) (van Gool and Cawood, 1994; Contardo et al., 2008; Contreras-Reyes et al., 2016). In particular, the SC Chilean continental margin currently falls within the classification of an accretionary margin: a slow convergence rate (6.6 cm/year; Angermann et al., 1999), and trench sediment thickness of ~2 km (Díaz-Naveas, 1999; Grevemeyer et al., 2003; Maksymowicz et al., 2017; Contreras-Reyes et al., 2017; Tréhu et al., 2019). However, the SC Chilean margin underwent a period of subduction erosion during the Miocene, when the convergence rate was > 8 cm/year and the trench sediment thickness was < 1 km (Kukowski and Oncken, 2006). A rapid increase of sediment supply to the trench in the Pliocene following a period of glaciation and a steady decrease of the convergence rate between the Nazca and the South American plates shifted the SC Chilean margin from erosive to accretionary (Melnick et al., 2006).

Seismic studies have reported the presence of an accretionary prism 30-50 km wide with P-wave velocities (V_p) of 2.5-5.0 km/s interpreted as unconsolidated (frontal prism) and semi-consolidated accreted (middle prism) sediments (Fig. 1; Moscoso et al., 2011; Contreras-Reyes et al., 2017). The landward edge of the interpreted accretionary prism is defined by an abrupt increase in seismic velocities and the location of the shelf break, defined as the transition from the continental slope to the shelf (Fig. 1; Contreras-Reyes et al., 2017; Tréhu et al., 2019a). The transition between the accretionary prism (frontal and middle prisms) and the continental framework (internal prism) is usually referred as the backstop and has been proposed to mark the up-dip limit of the seismogenic zone, inhibiting earthquake rupture propagation towards the trench (Contreras-Reyes et al., 2010; Moscoso et al., 2011). However, evidence for seafloor uplift along a profile crossing the patch of greatest slip during the 2010 Maule earthquake suggests at least localized up-dip activation of the interplate boundary beneath the accretionary prism during mega-thrust earthquakes, with important implications for the processes of tsunami generation and rheological behaviour of the continental wedge (Maksymowicz et al., 2017).

Generally, accretionary margins consist of a series of mostly trench-parallel accretionary thrust ridges that contain largely compressed, folded, and faulted turbidites and trench-fill deposits (Suess et al., 2018). These morphological features, characterized by relative seafloor uplift of up to hundreds of meters, have been observed in accretionary prisms worldwide such as in the Barbados Ridge accretionary complex (e.g. Brown et al., 1987), the Nankai accretionary complex (e.g. Park et al., 2002; Schumann et al., 2014), the southwestern Taiwan margin (e.g. Klaucke et al., 2016) and Cascadia (e.g. Hyndman et al., 1994; Tréhu et al., 1995, 1999; Fisher et al., 1999; Adam et al. 2004). The folding and thrusting around the accretionary ridges are usually associated with splay faulting across the trenchwardmost edge of the accretionary prism. Bottom simulating reflectors (BSR) are often present within these accretionary ridges and are associated with accumulation of free gas underneath possible gas hydrate formation, which might be interrupted by cold seep activity (seepage) (Brown et al., 1987; Tréhu et al., 2004a, 2004b; Klaucke et al., 2016). Mud diapirism and volcanism can occur as well in these compressional scenarios providing an important dewatering mechanism of the accretionary wedge (Brown et al., 1988; Kopf, 2002). Thrust faults may also act as dewatering pathways (Cloos, 1984; Klaucke et al., 2016).

Accretionary ridges have been found in the accretionary prism along the Chilean margin (e.g. across the accretionary prism off Golfo de Arauco and Penas; Contreras-Reyes et al., 2008 and Maksymowicz et al., 2012; respectively). Near the shelf break around the Maule Region, Geersen et al. (2011) identified accretionary thrust ridges that probably correspond to the superficial expression of active splay fault systems. In this study, we image the subsurface beneath a previously mapped (Geersen et al., 2011) N-S trending thrust ridge (Fig 3) that has been subject of investigation of small-scale structures like slumps, chemoherms, mud volcanoes, gas hydrate deposits, fluid migration path and seep sites (Grevemeyer et al., 2003; 2006; Flueh and Bialas, 2008; Klaucke et al., 2012; Villar-Muñoz et al., 2014). We present a shallow margin-parallel V_p model of the landward edge of the accretionary prism near the shelf break offshore SC Chile (35º-36ºS) based on controlled source seismic data. To evaluate the robustness of our results, the data were analysed using two different travel-time modelling techniques. We image the 3D P-wave structure of the upper ~4 km in the transition zone between the accretionary prism and the continental framework and discuss the implications of the model for local tectonics. Our results provide new insights into the interplay between the dynamics of accretionary structures and local distribution of fluid activity.

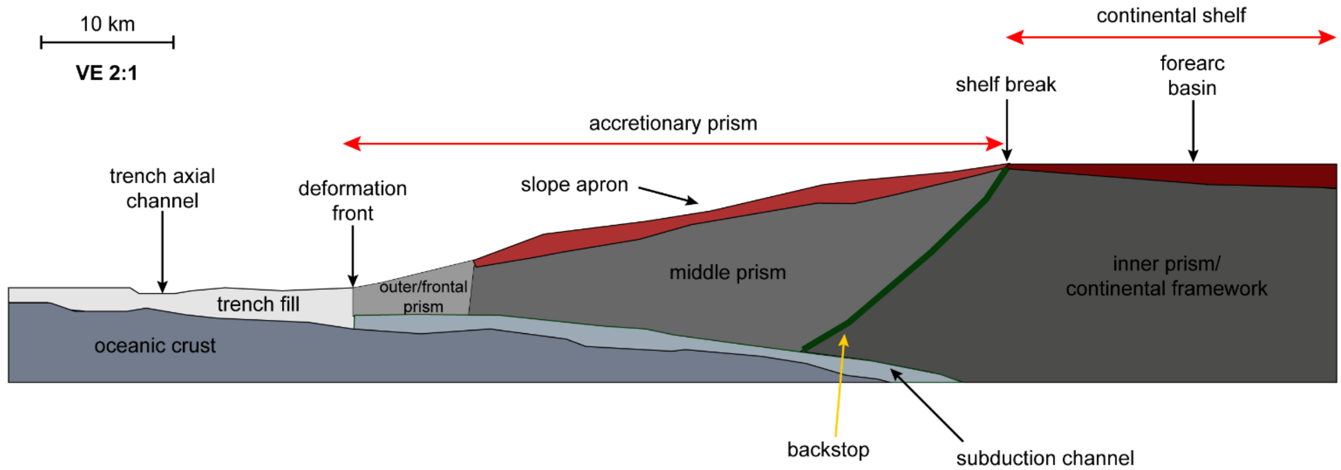

Fig. 1. Interpretative summary sketch of the southern-central Chilean margin for the Maule segment based on seismic studies (Moscoso et al., 2011; Contreras-Reyes et al., 2017). The accretionary prism is composed by the outer/frontal prism (poorly consolidated sediment) and middle prism (more compacted and lithified sediment). The continental framework rock (or inner prism) corresponds to the paleo-accretionary prism or continental basement (Contreras-Reyes et al., 2010). The solid dark green line indicates the accretionary Prism/Continental Framework Rock contact or backstop. Our study is located near the shelf break at the transition between the middle prism and the inner prism.

2. Tectonic Setting

The SC Chilean margin is controlled by the subduction of the oceanic Nazca Plate under the continental South American Plate at a current rate of 6.6 cm/year and a convergence azimuth of about 78° (Fig. 2; Angermann et al., 1999). The trench is filled with sediments 1-2.5 km thick (Völker et al., 2013) and is incised by a sinuous axial channel. The current accretionary regime (Bangs and Cande, 1997) is evident by the morphology of the forearc westernmost part which is characterized by a 30-50 km wide accretionary prism that can be subdivided into two main segments: (1) an outer accretionary wedge (5–10 km wide) characterized by low seismic velocities of <3.0 km/s, and interpreted as a frontal prism of poorly compacted and highly deformed sediments, and (2) the middle wedge (~50 km wide and V_p of ~4 km/s) interpreted as a middle prism composed by older, compacted and lithified sediment, overlain by an apron of low velocity slope sediments (Fig.1; Moscoso et al., 2011; Contreras-Reyes et al., 2017).

Our study area is located at the transition between the middle prism and the continental framework rock (Figs. 1-3). Seismically, this boundary has been characterized at depth by an abrupt lateral change in velocity from velocities characteristic of accretionary prism sediments (<4 km/s) to velocities of >5 km/s representing the continental framework rocks. The continental framework in this region has been interpreted to be a late metamorphosed Paleozoic subduction complex (Willner, 2005). Splay faults can be generated and intersect the seafloor forming thrust ridges in this transition zone in response to compression and shortening of the forearc (Moore et al., 2007). Formation of intra-slope basins with hemipelagic sediments is favoured by the existence of these ridges (Suess et al., 2018). In our study area, a thrust ridge system and associated intra-slope basins have been mapped (dashed pink line in Figs. 2, 3) and interpreted by Geersen et al. (2011) as the seafloor expression of the splay fault accommodation of subduction motion. Geersen et al., (2011) propose this thrust ridge as the boundary between the highly deformed accretionary prism and the continental shelf sedimentary cover overlying the continental framework.

Much of the SC Chilean margin is characterized by basal accretion and sediment underthrusting, e.g. at the NW of our seismic survey as evidenced by the seafloor morphology of the accretionary prism near the trench ("Reloca slide" in Fig. 3; Contreras-Reyes et al., 2016) and subduction channels of considerable thicknesses (Olsen et al., 2020). However, both frontal accretion and sediment underthrusting have also been observed (Contreras-Reyes et al., 2010; 2017; Tréhu et al., 2019a). Another bathymetric feature observed in this area corresponds to the Itata Canyon (Figs. 2, 3A), which incises the continental shelf; however, this system is not present at the lower continental slope (Geersen et al, 2011) and is thought to be inactive at present (Klaucke et al., 2012). Tréhu et al. (2019a) discuss tectonic implications of similar canyons (the Mataquito and Huenchullami canyons) that do not reach the trench between 34° and 35°S and attribute this to large scale disruption of the forearc due to subduction of topography.

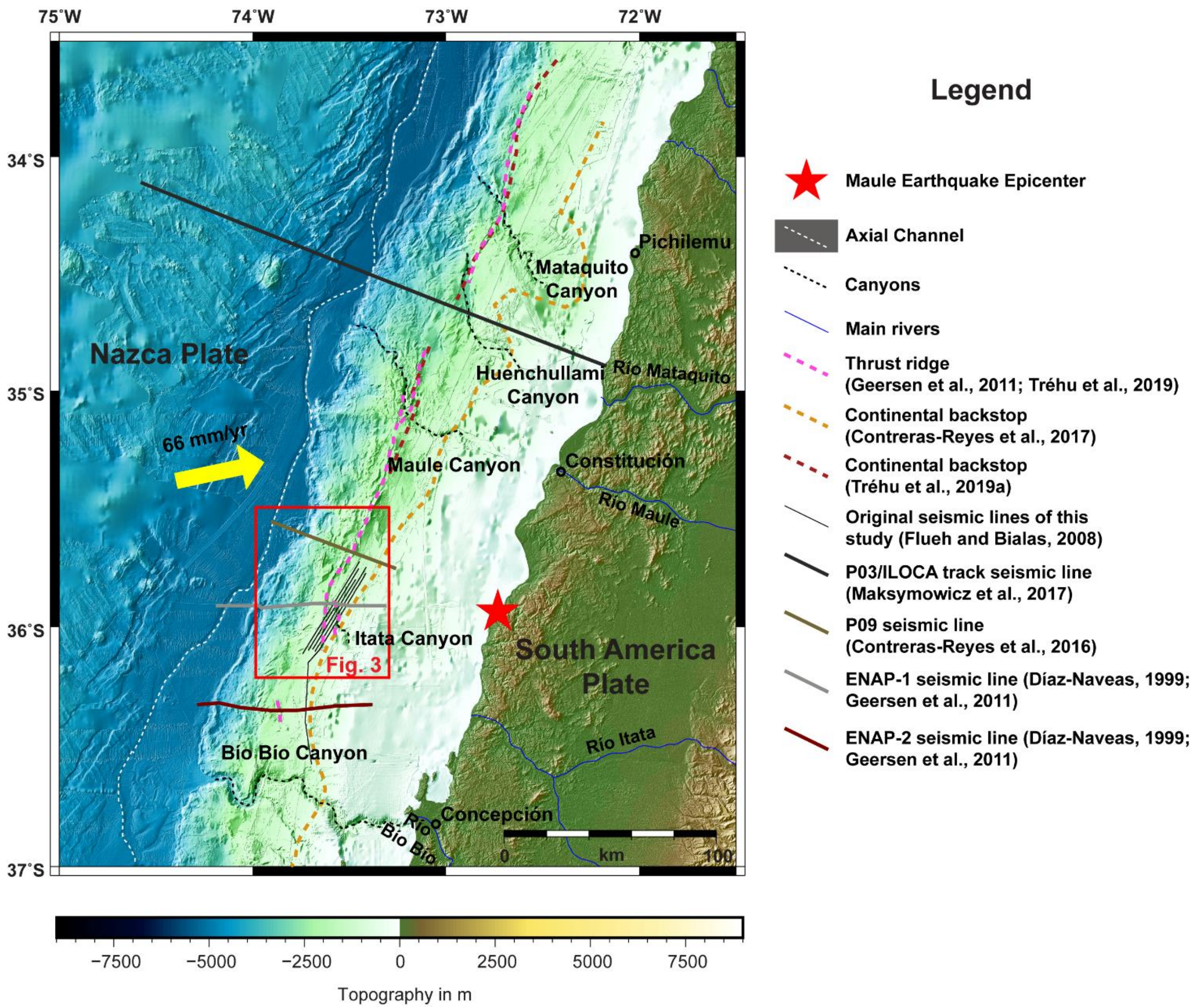

Fig. 2. South-central Chile bathymetry from the Global Multi-Resolution Topography (Ryan et al., 2009), version 3.6.6. Main oceanic bathymetric features are depicted. Convergence between the oceanic Nazca and the continental South American Plates

is indicated by the yellow arrow. Red contoured square encloses the location of the study area shown with more detail in Fig. 3. See the legend for further information.

Several authors have proposed the existence of fluid activity in accretionary ridges in SC Chile. Klaucke et al., (2012), using sidescan sonar mapping and seafloor observations, reported the occurrence of both fossil and likely active cold seeps. As suggested, chemoherms (carbonate structures) and buried seeps encountered in our study area were partially formed or have been overprinted by fluid venting and biogenic formation probably generated within the slope sediments (Fig. 3). However, Klaucke et al. (2012) propose little current activity, although either much higher fluid fluxes in the past or fluid flows over prolonged periods may explain the observations. On the other hand, bottom simulating reflectors (BSR) are often present in accretionary margins and are commonly associated with the occurrence of gas hydrates on the continental slope. Heat flow anomalies derived by BSR depth calculation of geothermal gradients have been obtained in the vicinity of our study area (Grevemeyer et al., 2003; Villar-Muñoz et al., 2013) with values >35 mWm^{-2}, indicating advective fluid migration along stratigraphic boundaries or fault zones (Fig. 3). Grevemeyer et al. (2006) calculated heat flow anomalies from ODP Leg 202 drillcore data along a transect that intersects our profiles with values up to ~120 mWm^{-2} (Fig. 3).

Seismic reactivation of splay faults occurred 12 days after the 2010 Maule megathrust earthquake M_w 8.8 in the Pichilemu area (34.5° S; Farías et al., 2011; Ruiz et al., 2014). Using a local marine network, some seismic activity was detected mainly near the boundary between the active accretionary prism and continental basement as a post-seismic response of the outer accretionary wedge updip from the patch of greatest slip during the 2010 M_w 8.8 Maule earthquake (Tréhu et al., 2019b). In contrast, little post-seismic activity was observed in the accretionary prism and along the splay faults around our study area (See Fig. 1 in the Supplementary material, section A1; Moscoso et al., 2010; Lange et al., 2012; Contreras-Reyes et al., 2017). Lieser et al. (2014) proposed the existence of a stable accretionary prism to explain the progressive decrease in post-seismic splay fault response south of ~36°S.

3. Seismic Modelling

3.1. Wide-Angle Seismic Data

Seismic data were acquired by the German IFM-GEOMAR Institute for Marine Sciences (now GEOMAR Helmholtz Centre for Ocean Research Kiel) during cruise JC23 on the RRS JAMES COOK in 2008. The experiment comprised five parallel wide-angle seismic profiles spaced ~1.5 km apart with strike of N31.5°E and maximum length of 50 km (Fig. 3). Spatially coincident deep towed sidescan data were also acquired. The source was 3 GI airguns each equipped with 250 cu-inch generator and 105 cu-inch injectors were shot at 13 sec intervals providing an average shot spacing of ~20 m (Flueh and Bialas, 2008). Along the central line, 11 OBS/H (Ocean Bottom Seismometers/Hydrophones) were deployed on the seafloor at a depth of ~1500 m. However, due to low signal to noise ratios on the geophones, we only used data from the 3 OBHs and from the hydrophone component of 6 OBSs for further processing and modelling (Fig. 3). A 4-channel surface streamer (300 m long) also recorded the shots.

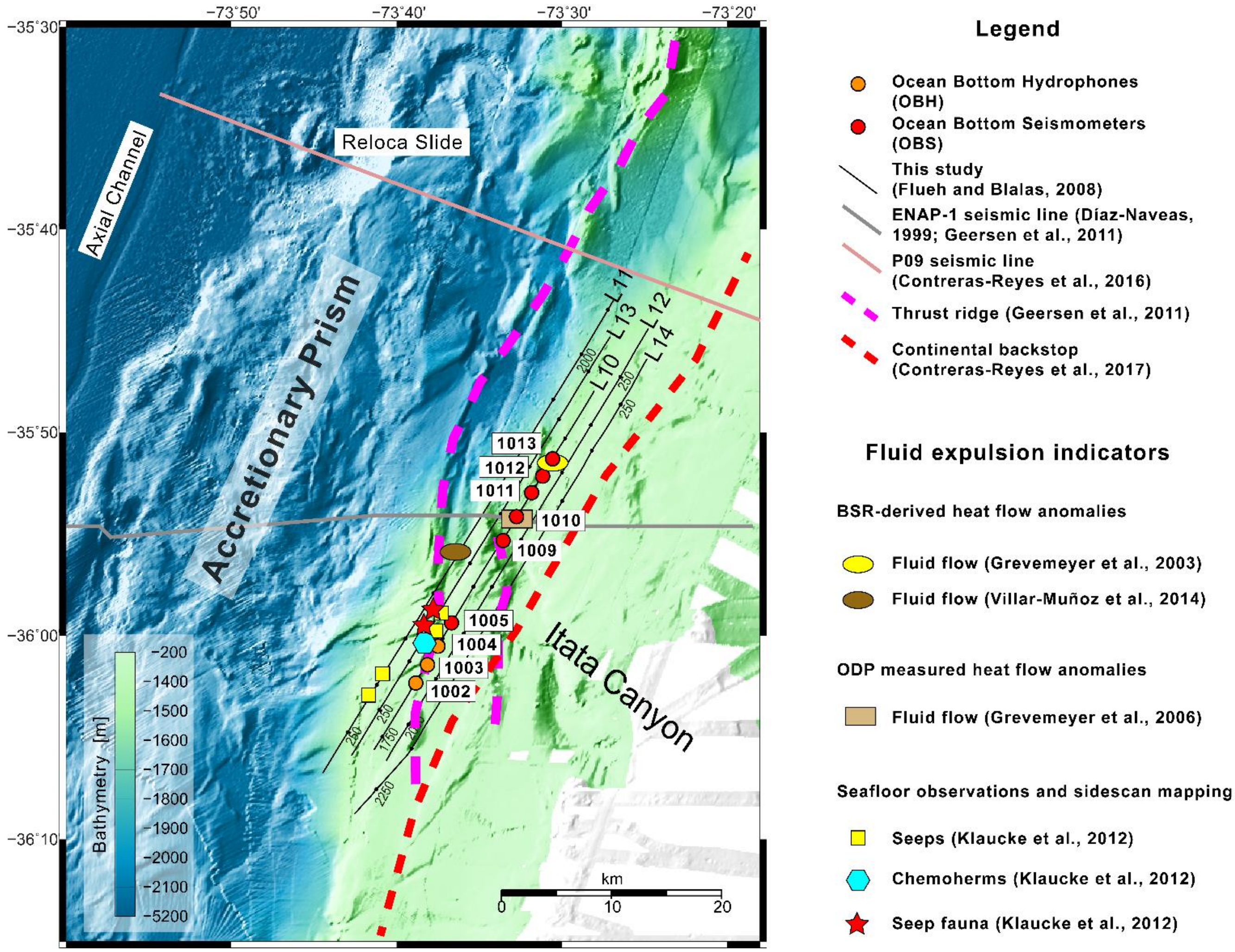

Fig. 3. Study area, experiment geometry, main bathymetric and tectonic features, and seepage activity. The high-resolution bathymetric image of the seafloor off Maule region was collected during the cruise JC23 on the RRS JAMES COOK (Flueh and Bialas, 2008). Red and orange circles indicate the 9 used stations and thin black lines correspond to the wide-angle seismic refraction profiles (L10, L11, L12, L13, L14) processed in this study whose gunshot locations are numbered every 250 shots (black dots along the profiles). Solid thick lines depict locations of P09 (Contreras-Reyes et al., 2016) and ENAP-1 profiles (Geersen et al., 2011; see Fig. 2 for the whole extent). The N-S/NE-SW trending Thrust Ridge (dashed pink line) is clearly visible by its bathymetric signature whose location coincides with thrust splay faults visible along ENAP-1 profile (Geersen et al., 2011). Fluid expulsion indicators and their locations are also shown.

Seismic data examples recorded at four instruments from shots along profile L10 are shown in Fig. 4. A strong hyperbolic signal centred on the instrument corresponds to the water wave arrival. At greater offsets, first arrivals were identified and classified into two groups based on their distinct slope: low velocity sedimentary phases (P_s) and deeper sedimentary phases (P_g). The character of the data shows a strong triplication suggesting an abrupt increase in velocity at a boundary between the layer producing phases P_s and the one producing P_g .

A total of ~13,000 first arrivals were picked. Direct water wave arrivals were not picked because acquired high-resolution bathymetry constrain the seafloor depth and pre-processing aboard the cruise was already done in order to relocate the instrument positions. Pick uncertainties were estimated to be 60 ms. Experiment geometry and poor signal propagation limited the picking of arrivals with offsets longer than 15 km, limiting the maximum depth of penetration to ~4 km.

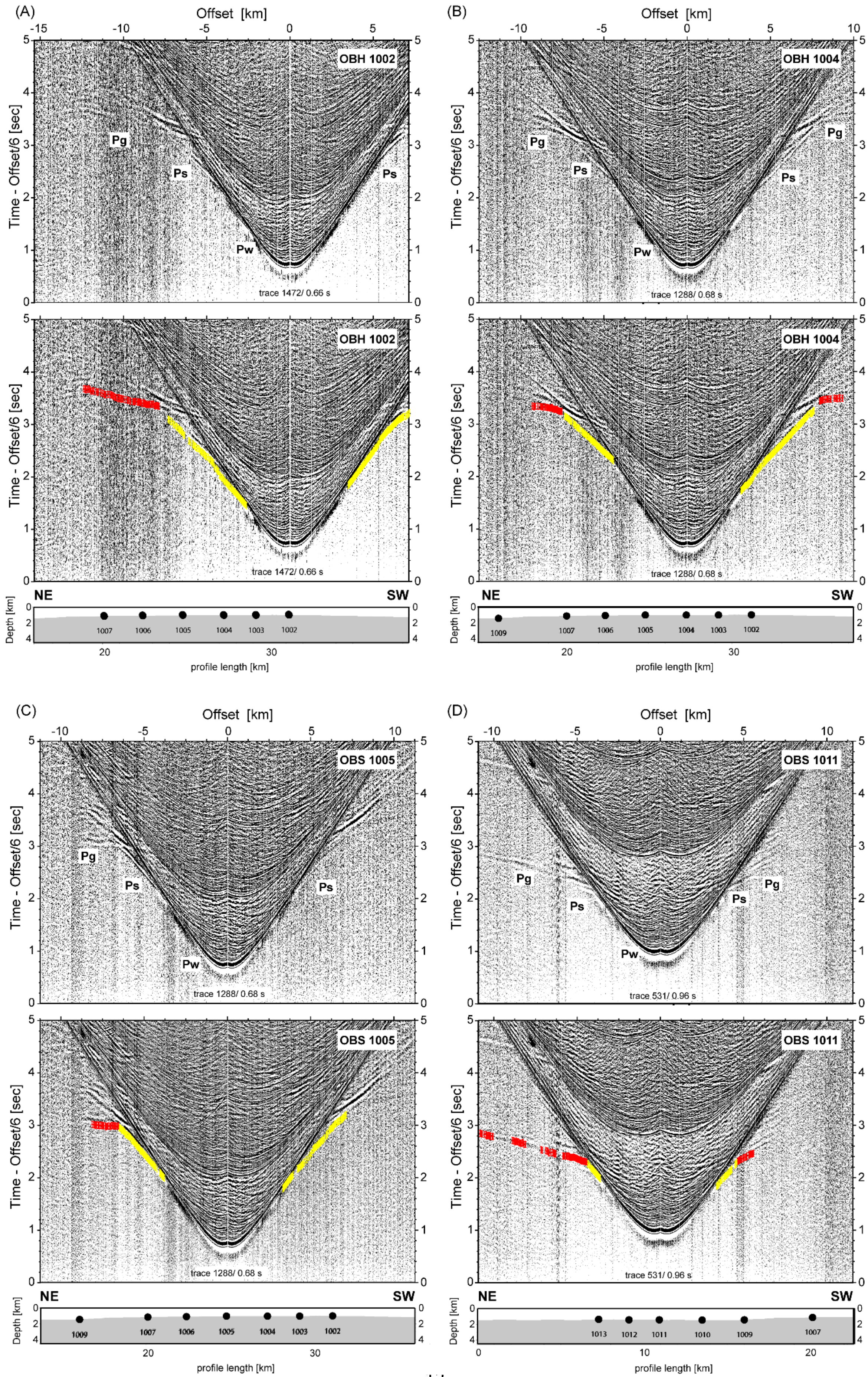
(A)
Offset [km]
Time - Offset/6 [sec]
OBH 1002
Pg
Ps
Pw
trace 1472/ 0.66 s
NE
SW
Depth [km]
profile length [km]
(B)
OBH 1004
trace 1288/ 0.68 s
(C)
OBS 1005
trace 1288/ 0.68 s
(D)
OBS 1011
trace 531/ 0.96 s

Fig. 4. Seismic record examples along profile L10 recorded at (A) OBH 1002, (B) OBH 1004, (C) OBS 1005 (respective hydrophone channel) and (D) OBS 1011 (respective hydrophone channel). For each seismic record, the upper panel shows the corresponding travel-time section using a reduction velocity of 6 km/s and the detected first-arriving P waves refractions are indicated: P_w (water wave arrival), P_s (low velocity sedimentary phase) and P_g (deeper sedimentary phases). Corresponding picked phases (P_w excluded) and respective uncertainties are shown in the middle panel: yellow dots denote P_s phases and red dots denote P_g phases. Lower panel shows the location of the instruments along profile L10. For seismic records examples along profiles L11, L12, L13 and L14, see Fig.2 in the Supplementary Material, Section A2.

3.2. Three-Dimensional Travel-time Tomography

Travel-time inversion and 3-D ray tracing in a heterogeneous media was computed using the tomographic software package TOMOLAB/STINGRAY (Toomey et al., 1994). A 31.5° rotated Cartesian coordinate system was used for defining a slowness model, which was parameterized as a 10 x 54 x 8 km^3 gridded volume with a cell size of 100 m in all directions. A minimum-structure initial model was constructed through 3-D extrapolation by hanging a 1-D velocity depth profile from the seafloor (Fig. 5). This 1-D model was derived by 1-D forward modelling of travel times along the central profile L10 and is characterized by V_p values of 1.6 km/s at the seafloor.

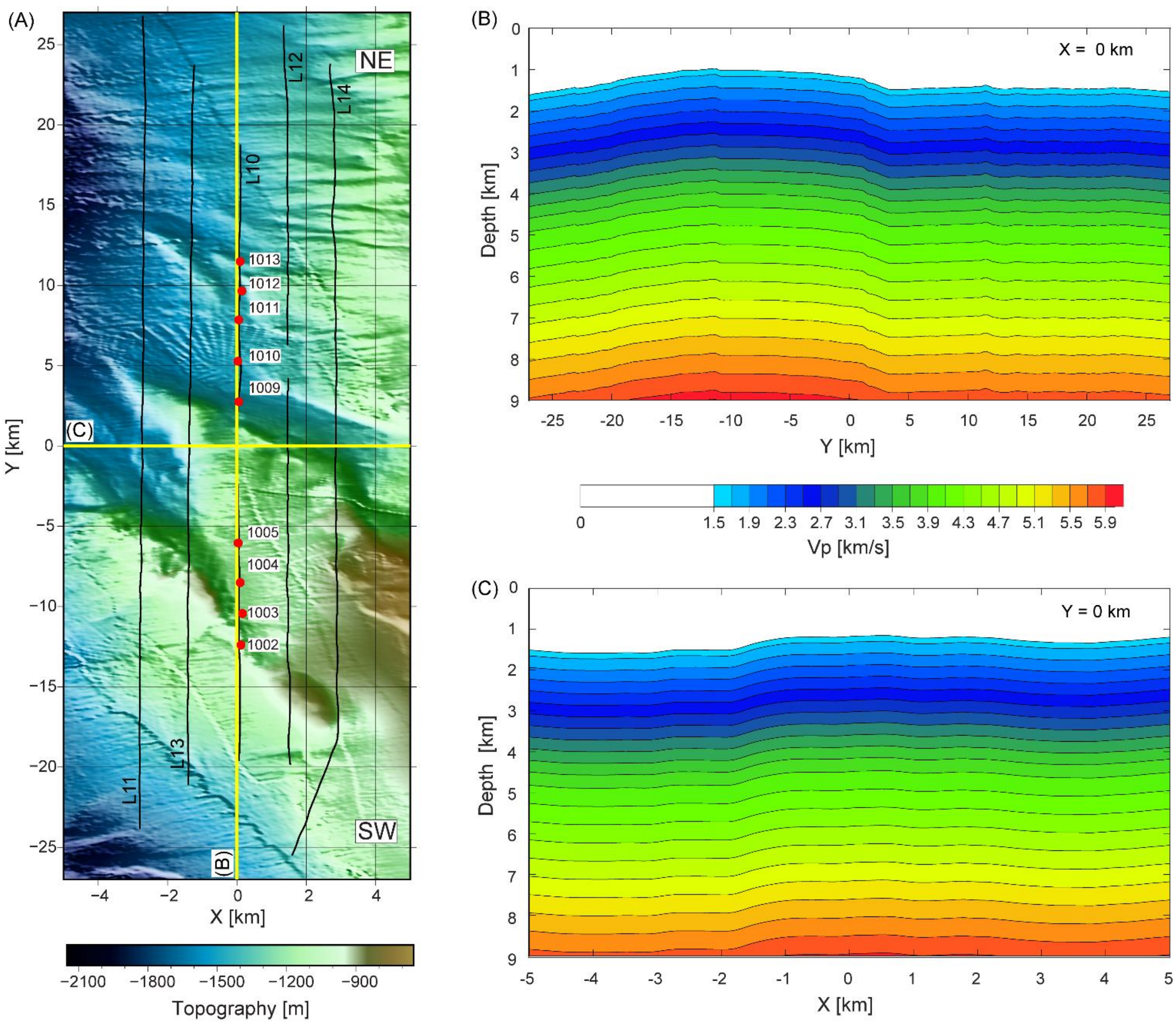

Fig. 5. Experiment geometry and 2D example slices of the 3D initial velocity model used for travel-time inversion using STINGRAY/TOMOLAB software package (Toomey et al., 1994). (A) Experiment setting using Cartesian coordinate

projection with 31.5° rotation angle with respect to north. Small black dots correspond to airgun shots along profiles L10, L11, L12, L13 and L14. Red dots represent the 9 seismic stations used in this study. Yellow lines indicate the location of the slices depicted in (B) and (C). (B) Initial velocity model along Y axis at X=0 km. (C) Initial velocity model along X axis at Y=0 km.

This inversion approach allows the definition of a perturbational model with its associated uncertainty and the subjective choice of several inversion parameters (Toomey et al., 1994). The ill-conditioned inversion problem requires a regularization which minimizes an objective function for the 3D iterative process that penalizes the roughness and size of the slowness perturbations with respect to the 3D starting model. Inversion constraints (penalty function, horizontal and vertical smoothing) are applied to the perturbational model and then normalized to remove bias (Toomey et al., 1994).

In this case, we defined a uniform node spacing of 200 m and maximum perturbation at each node of 0.05 (fractional uncertainty) for the perturbational model. We assumed an isotropic medium due to limited azimuthal ray coverage and adopted a "jumping strategy" for the 3-D tomographic inversion of first arrivals. Thus, the model constraints are operative on the total perturbation expressed with respect to the starting model (Toomey et al., 1994). implying a rather conservative approach. Several tests were computed (~50 tests) to obtain an appropriate data misfit.

The final 3-D model was obtained using a penalty function λ_p of 0.01 and vertical and horizontal smoothing factors (λ_z, λ_{xy}, respectively) of 200 and 400, respectively, resulting in an RMS data misfit of 38 ms after five iterations. Each iteration comprised a total of 3,000 LSQR iterations. A shallow ray coverage, which is a function of the velocity structure as well as of the acquisition geometry, results in shallow imaging (< 6 km); however, several model features are identified and give insights into the relationship between the velocity structure and local tectonics.

3.3. Results

3.3.1. Three-Dimensional Results

Figs. 6 and 7 depict vertical model slices along the Y and X axes, respectively, and Fig. 8 shows subhorizontal slices parallel to the seafloor (along Z axis). The final velocity model is masked using a spatially averaged DWS (Derivative Weight Sum) calculated as the weighted sum of all ray path lengths influenced by any model parameter (Toomey et al, 1994). Overall, observed P-wave velocities in the range of 1.7-4 km/s are consistent with the sedimentary nature of the middle accretionary prism (Moscoso et al., 2011; Contreras-Reyes et al., 2017). The obtained velocity gradient is smoother than expected for the abrupt boundary between the sediments and underlying material with velocity ~4 km/s suggested by the strong triplication of the seismic records. Near the seafloor, lower velocities (<1.7 km/s, shown in cyan colours in Figs. 6, 7 and 8) are observed mainly in the south-west area, which corresponds to the thrust ridge location identified by Geersen et al. (2011). Velocities < 1.5 km/s (even lower than 1.4 km/s, depicted as white spots within ray-covered areas in Figs. 6, 7 and 8) have been observed by several authors in similar shallow hydrate-bearing sedimentary environments (Arsenault et al., 2001; Hornbach et al., 2003; Schumann et al.,2014) and interpreted to indicate the presence of free gas in the sediment pore space. However, several tests are performed to assess if the 3D model is capable of resolving these features with a special focus on the central line (see Figs. 9 and 10 for uncertainty estimates and resolution tests). In contrast, both the near-seafloor velocity (> 1.9 km/s) and the velocity gradient are larger to the northeast (with a value of ~1.0 s^{-1}), which may reflect a less perturbed sedimentary sequence over a more compact and lithified accretionary wedge. The highest V_p values (~5 km/s) are present to the northeast at Y=5-10 km and a depth of 4 km below the sea surface, although it is poorly resolved (Fig. 6).

The first-order correlation between lower shallow sedimentary P-wave velocities and the thrust ridge location extends across the entire imaged volume (Figs. 6, 7 and 8). Besides, stronger velocity gradients below Z=1 km and Y > 0 km (seen in Figs. 6, 7D, 7E, 8C and 8D) are also correlated to the associated splay fault system imaged by Geersen et al., (2011) along the ENAP-1 profile (Fig.3).

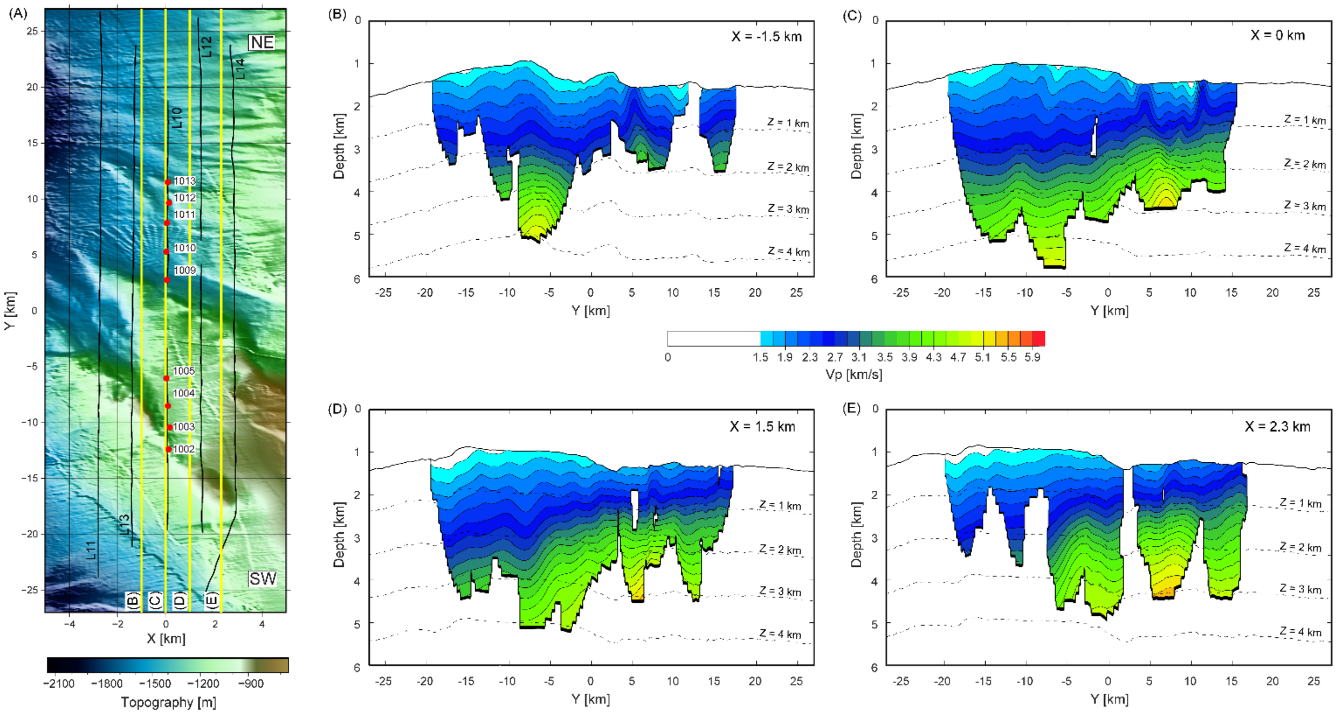

Fig. 6. Vertical slices through the final 3D velocity model along Y axis. (A) Experiment setting using Cartesian coordinate projection with 31.5° rotation angle with respect to north. Small black dots correspond to airgun shots along profiles L10, L11, L12, L13 and L14. Red dots represent 9 seismic stations used in this study. Velocity model slices at (B) X= -1.5 km, (C) X = 0 km. (D) X = 1.5 km and (E) X =2.3 km, are shown and their map location is indicated by yellow straight lines in (A). Dashed lines indicate iso-surfaces along Z axis which is defined relative to the seafloor.

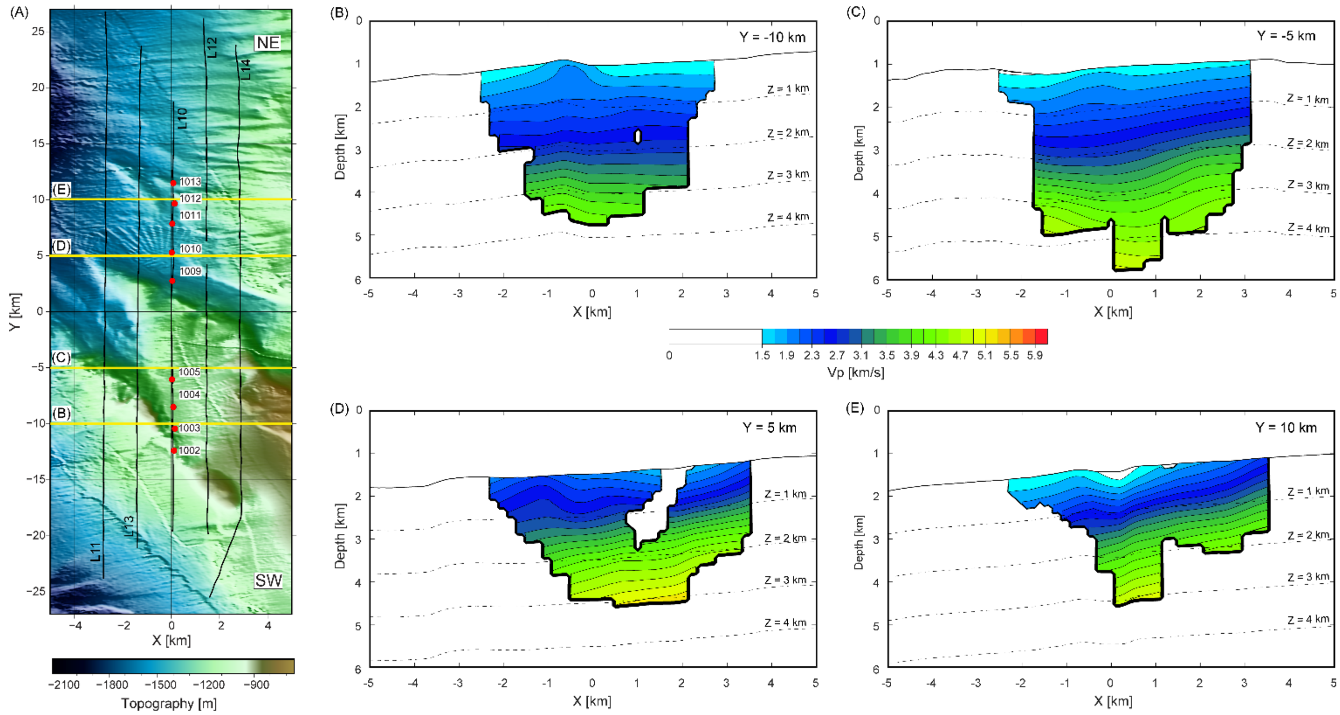

Fig. 7. Vertical slices through the final 3D velocity model along X axis. (a) Experiment setting using Cartesian coordinate projection with 31.5° rotation angle with respect to north. Small black dots correspond to airgun shots along profiles L10, L11, L12, L13 and L14. Red dots represent 9 seismic stations used in this study. 2D velocity model slices at (B) Y= -10 km, (C) Y = -5 km. (D) Y = 5 km and (E) Y =10 km, are shown and their map location is indicated by yellow straight lines in (A). Dashed lines indicate iso-surfaces along Z axis which is defined relative to the seafloor.

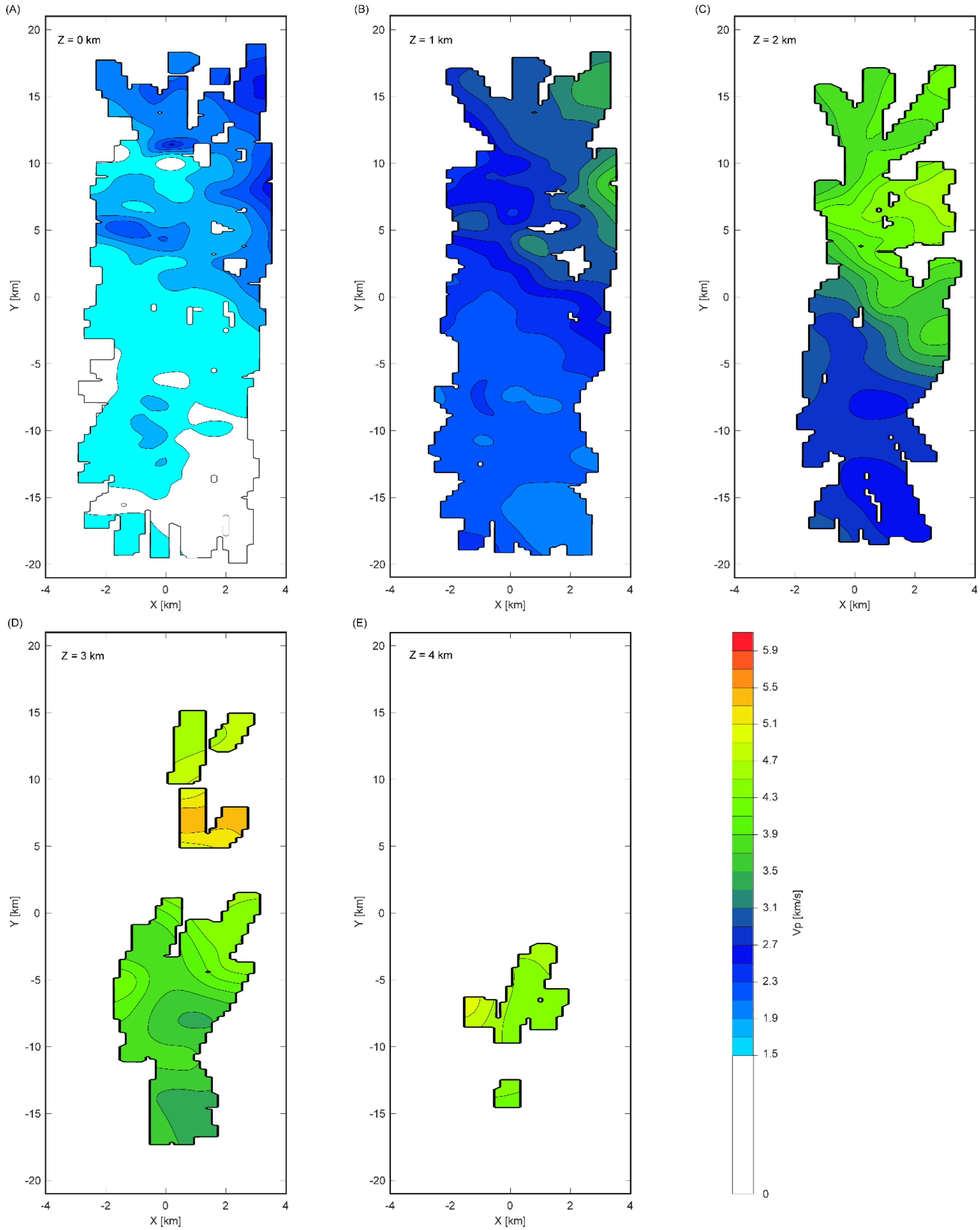

Fig. 8. Seafloor-parallel slices through the final 3D velocity model at (A) Z=0 km, (B) Z= 1 km, (C) Z= 2 km, (D) Z = 3 km

and (E) Z = 4 km, where Z is positive downwards, starting from the seafloor. These iso-surfaces are also shown in the vertical slices depicted in Figs 6 and 7. The coordinate system coincides with that of Figs. 5-7.

To assess the accuracy and resolution of the 3D model, we performed a Monte Carlo uncertainty analysis and synthetic recovery tests. The Monte Carlo analysis was carried out by generating several perturbed initial velocity models (±5% amplitude applied to the starting velocity model) and corresponding travel time sets with added random noise (±100 ms). Running corresponding inversions with the same parameters of our final model allowed us to compute the average and standard deviation of the output ensemble. Results are shown in Fig. 9. Areas with dense ray coverage (e.g., right below the instruments and in the middle portion of the south-western part of the model), show lower uncertainty values (<0.01 km/s) whereas the north-eastern part of the model shows comparatively higher uncertainty values (>0.01 km/s) (Fig. 9A, 9C). Standard deviation values show a general increase with depth and towards the edges of the model, reaching maximum values around the high velocity zone at around 35 km distance (~0.2 km/s). Over most of the very low velocity zones with V_p < 1.5 km/s (white spots in the average velocity model shown in Fig. 9B), the uncertainty values are higher than 0.02 km/s, implying a possible underestimation of those velocities within that range.

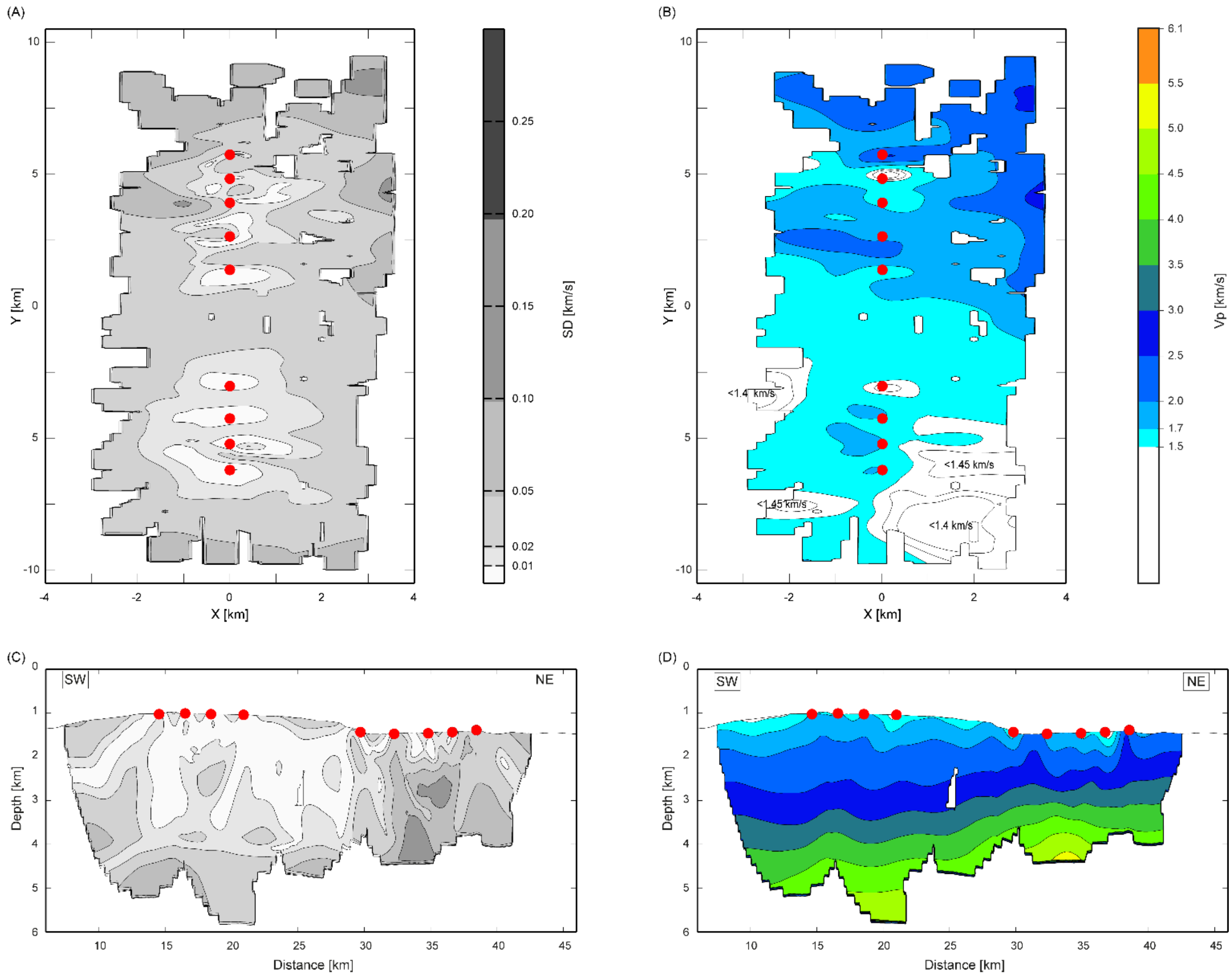

Fig. 9. Monte Carlo tests for the 3D velocity model. (A) Standard deviation model along the seafloor-parallel slice at Z=0 km, i.e., at the seafloor. (B) Average velocity model at the seafloor. (C) Standard deviation on a vertical slice at X=0 km, roughly coincident with central seismic profile L10. Distance in km is calculated from the negative end of the Y-axis in (A) and (B), that is, an offset of 27 km is considered. (D) Average velocity model from the vertical slice shown in (C).

Pseudo checkerboard tests were done by superimposing elliptical Gaussian anomalies of a ±5% maximum amplitude on the final velocity model across the vertical slice depicted in Fig. 6C, which is coincident with the central line L10 (see Fig. 3 for profile location). These anomalies were then prolonged along the X-axis crossing the entire 3D volume as horizontal elliptical cylinders. The distribution and sizes of the anomalies across the central vertical slice are shown in Fig. 10A. The recovery results depicted in Fig. 10B show that, as expected, the resolution is best near the central part of the model and decreases towards the edges of the model. Although most of the anomalies are recovered, significant vertical smearing is present. High velocity anomalies are relatively better resolved and less affected by the smearing effects. Due to the smearing, the anomalous low velocity zones (<1.5 km/s) may be inversion artifacts due to the presence of a deeper low velocity layer which has smeared up to the surface. This effect is even stronger at greater depths where the velocity contrast is presumably higher. The model is not capable of resolving the abrupt boundary already discussed.

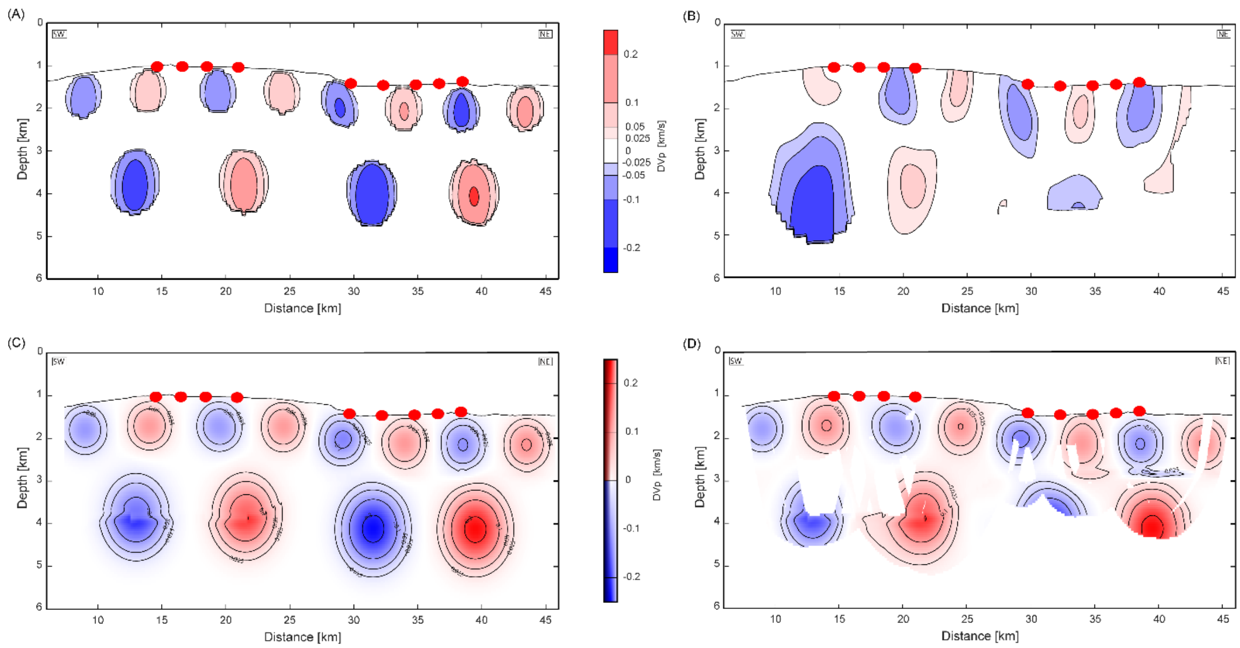

Fig. 10. Synthetic resolution tests. Distance in km is calculated from the negative end of the Y-axis in Figs. 6 and 7, that is, an offset of 27 km is considered. Red circles indicate the instrument locations. (A) Synthetic velocity structure from the 3D model along the vertical slice along Y axis at X=0 km, which is roughly coincident with the central line L10. (B) Recovery results from the vertical slice shown in (A) masked according to the final velocity model. Note the significant smearing effects on the anomaly recovery. (C) Synthetic velocity structure from the 2D model along the central line L10 with an analogous geometry as in (A). (D) Recovery results from the 2D model shown in (C). Overall, the anomalies are better recovered in shape and amplitude than the 3D model results, albeit the transition zone shows some smearing.

3.3.2. Two-Dimensional Results along central line L10

To evaluate the robustness of our 3D model and improve some of its limitations along the central line, we also generated a 2-D velocity-depth model using the joint refraction/reflection 2-D tomographic inversion code of Korenaga et al. (2000) and additional a-priori information to generate a more complex starting model. For this analysis, we used the first arrival picks from the central profile L10 (Fig. 4), comprising a total of 2,920 picks (1,800 P_s phases and 1,120 P_g phases). Fig. 11A shows the 2D model results and Fig. 11B shows a velocity difference model between this 2-D model and the nearly coincident vertical model slice extracted from the 3-D model (Fig. 6C).

In general, the 2-D velocity structure along the central profile agrees well with the corresponding model slice from the 3-D model results in the upper 2 km (Fig. 11B). This is not surprising since the 3D model shows little variation across the X-direction that could bias the 2D interpretation of the 3D structure (Figs. 6, 7 and 8). The primary model features discussed in the previous section are observed in the 2D model: consistently lower shallow velocities in the southwest region and an increased vertical velocity gradient extending to the northeast (Fig. 11A). Greater discrepancy in the upper 2 km is observed at ~30 km where the high velocity feature observed in both models is resolved with higher amplitude (>0.5 km/s) in the 2D model (Fig. 11B). The large discrepancy at depth ($|DV_p|$> 0,5 km/s) reflects the smooth initial model and smoothing parameters used for the 3D model, which do not resolve the abrupt velocity contrast suggested by the triplication observed in the data. For the 2D modelling, the starting model was more realistic and the modelling approach allowed for a discontinuity. Fig. 11D shows a good data fit of both phases and the position of the critical point.

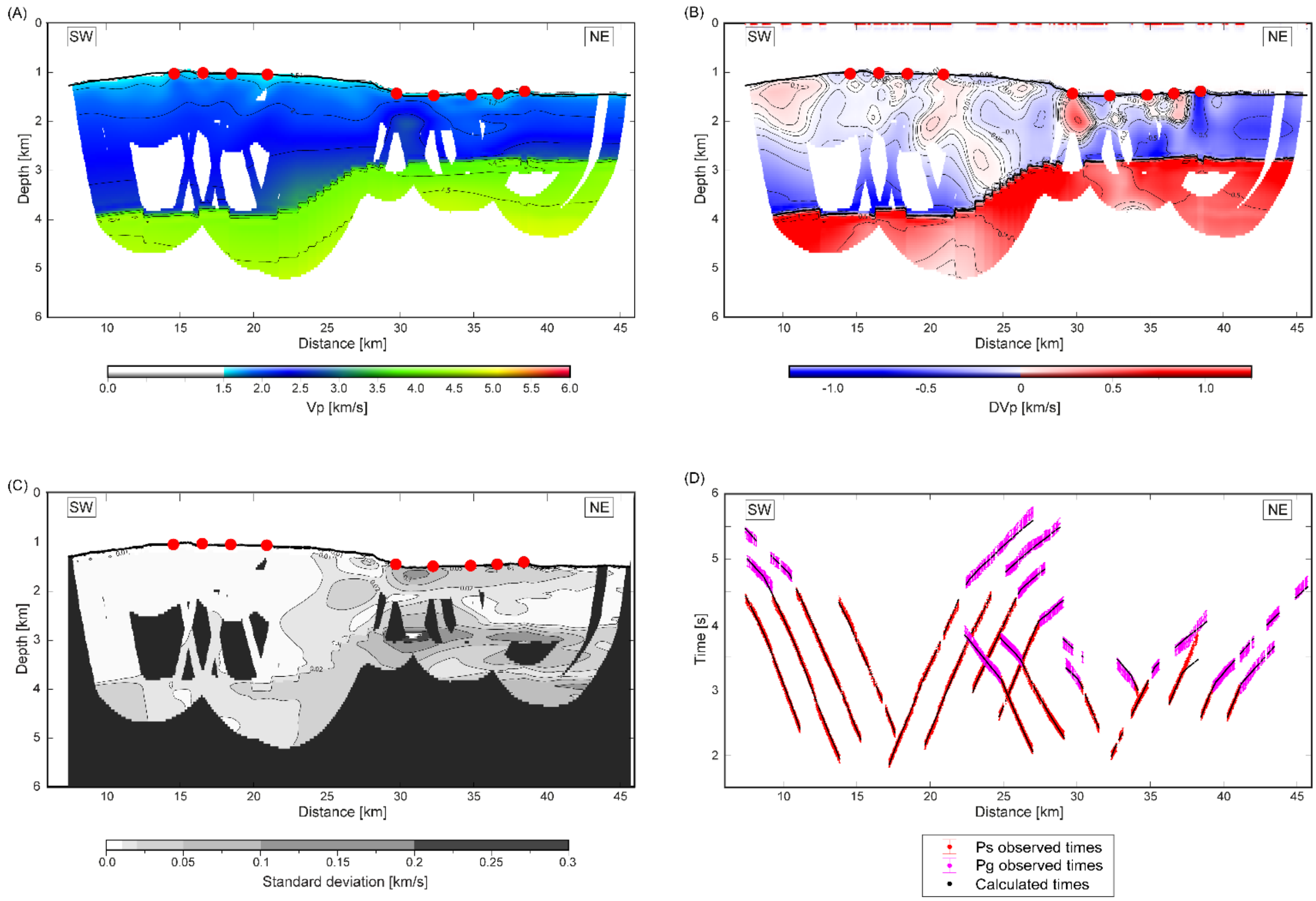

Fig. 11. Direct comparison of velocity-depth models along central line L10 (Figs. 6 and 7) of the study area and accuracy and data fitting of the 2D model. Distance in km is calculated from the negative end of the Y-axis in Figs. 6 and 7, that is, an offset of 27 km is considered with respect to Y-axis. (A) 2D velocity model obtained by travel time inversion of first-arriving P-waves collected along profile L10 using the joint refraction and reflection travel time tomography code of Korenaga et al., (2000). (B) Velocity difference model between the 2D model and the final 3D velocity model along Y axis at X=0 km, roughly coincident with central seismic profile L10. (C) 2D velocity uncertainty model for the final model shown in (B), using the Monte Carlo analysis. Higher deviation values, up to ±0.2 km/s (darker grey zones), are found at the bottom of the model and as localized patches at the northeast. (D) Travel time fitting for the 2D model. Observed times and associated picking uncertainty used for the 2D modelling (0.06 s for P_s phases and 0.08 s for P_g phases) are indicated by red and magenta dots with their corresponding error bars, respectively. Calculated times (black dots) are obtained from the 2D final model shown in (B). Final RMS data misfit are 53 and 69 ms for P_s and P_g phases, respectively. Poor fitting of P_g phase at OBS 1010 (at X~37 km) is consistent with higher uncertainties of the 2D model along the corresponding travel paths.

In order to assess the accuracy of the 2D seismic velocity model, we conducted a Monte Carlo uncertainty analysis (Korenaga et al., 2000) in a similar fashion to the 3D case, to estimate the uncertainty of our model parameters: our starting velocity model and smoothing constraints. This uncertainty parameter of the calculated V_p is better constrained in the southwest region with most of the values lower than 0.01 km/s whereas most of the northeast region values are higher than 0.02 km/s and several patches of increased values (up to ±0.1 km/s) are present (Fig. 11C). Resolution tests show lower vertical smearing effects than in the 3D case (Fig. 10D). Poorer recovery coincides with the position of the abrupt velocity gradient (Fig. 10D); however, it is very localized and is correlated with comparatively higher uncertainty values (>0.02 km/s) (Fig. 11C). It also noteworthy that $V_p <$ 1.5 km/s are not present in the 2D results (Figs. 11A, 11C).

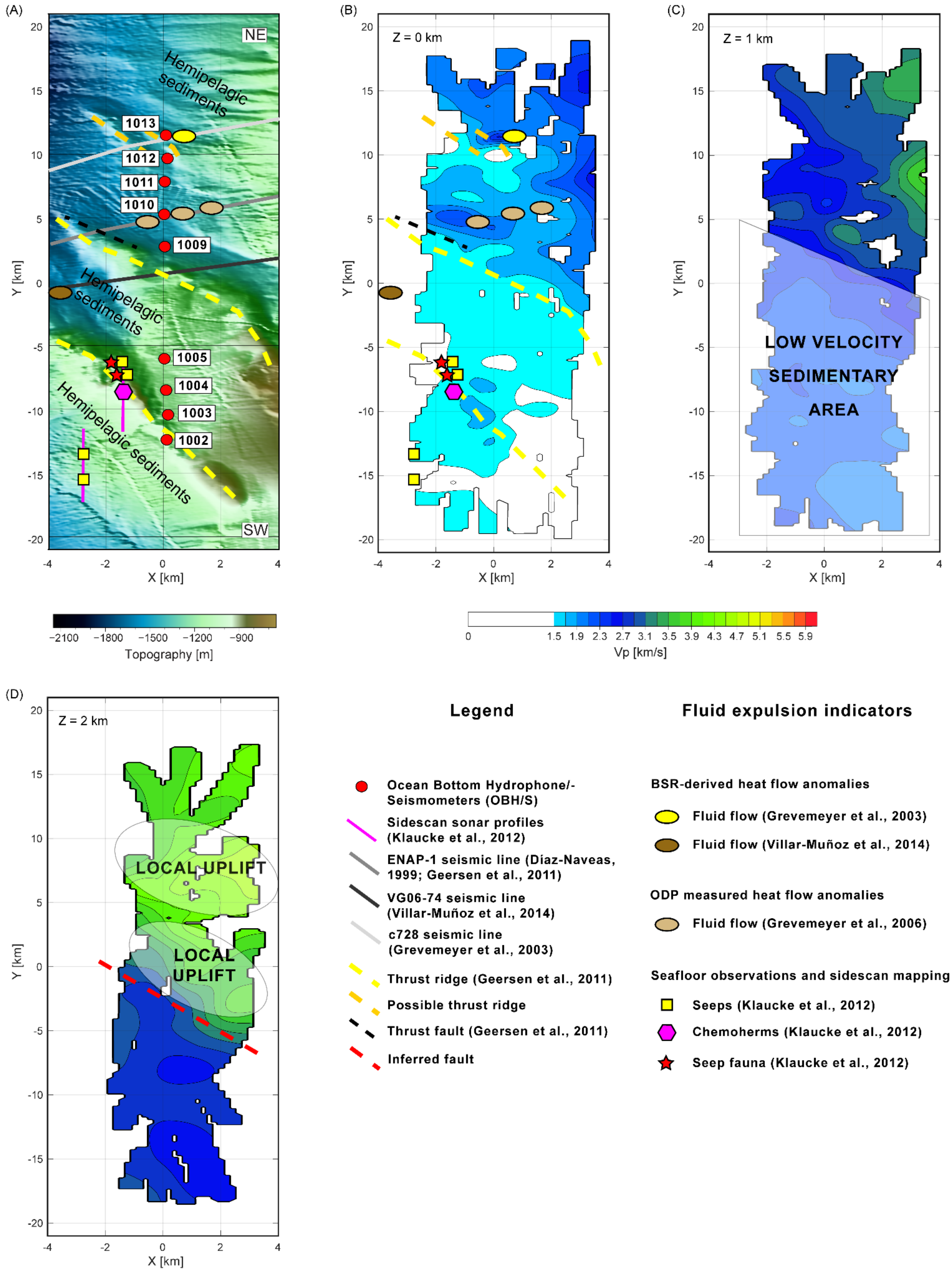
(A)
NE
SW
Hemipelagic sediments
Hemipelagic sediments
Hemipelagic sediments
1013
1012
1011
1010
1009
1005
1004
1003
1002
Y [km]
X [km]
Topography [m]
−2100 −1800 −1500 −1200 −900
(B)
Z = 0 km
(C)
Z = 1 km
LOW VELOCITY SEDIMENTARY AREA
Vp [km/s]
0 1.5 1.9 2.3 2.7 3.1 3.5 3.9 4.3 4.7 5.1 5.5 5.9
(D)
Z = 2 km
LOCAL UPLIFT
LOCAL UPLIFT
Legend
Ocean Bottom Hydrophone/-Seismometers (OBH/S)
Sidescan sonar profiles (Klaucke et al., 2012)
ENAP-1 seismic line (Díaz-Naveas, 1999; Geersen et al., 2011)
VG06-74 seismic line (Villar-Muñoz et al., 2014)
c728 seismic line (Grevemeyer et al., 2003)
Thrust ridge (Geersen et al., 2011)
Possible thrust ridge
Thrust fault (Geersen et al., 2011)
Inferred fault
Fluid expulsion indicators
BSR-derived heat flow anomalies
Fluid flow (Grevemeyer et al., 2003)
Fluid flow (Villar-Muñoz et al., 2014)
ODP measured heat flow anomalies
Fluid flow (Grevemeyer et al., 2006)
Seafloor observations and sidescan mapping
Seeps (Klaucke et al., 2012)
Chemoherms (Klaucke et al., 2012)
Seep fauna (Klaucke et al., 2012)

Fig. 12. Tectonic interpretation and 3D map view sections shown in Fig. 8. (A) Experiment setting whose coordinate system coincide with that of Figs. 6-8. Bathymetry and structural observations inferred by seismic reflection lines (coincident with seismic refraction profiles from this study (Flueh and Bialas, 2008) and ENAP-1 (Geersen et al., 2011)). Fluid activity indicators are also shown. The location of the thrust ridge and these fluid activity features are also overlain in map view section at Z = 0 km, (B), coincident with the seafloor, for better understanding. Note that these accretionary features and fluid activity related processes correlate with lower seismic velocities (< 2 km/s) while less perturbed sediment layers mainly located to the northeast present relative higher seismic velocities (around 2 km/s). (C) Map view section at Z = 1 km depth, although with less resolution indicates that the perturbed sedimentary area coincident with the thrust ridge shows lower seismic velocities. (D) Map view at Z = 2 km agrees well with the aforementioned correlation and also indicate probable local uplift along splay faults based on strong velocity contrasts.

4. Discussion

The three-dimensional results characterize the shallow sedimentary structure of the accretionary complex in a transition zone to the continental framework rock based on the experiment location with respect to the continental backstop (Fig.1-3). Comparison with 2D results along the central line shows that the velocity structure is primarily two-dimensional (Fig. 11A, 11B) showing a spatial correlation between lower velocity zones in the near-surface and the location of thrust ridges. Even though only shallow ray coverage is achieved, possible local uplifts at ~30 km and ~40 km along profile L10 (Fig. 11A), are inferred by noteworthy lateral velocity gradients (Fig. 12D). This feature correlates with the splay fault system that produces the observed thrust ridges and that probably extends deeper within the framework rock (Geersen et al., 2011). Overall, the near-surface velocity structure is better represented by the 2D model, which results in lower uncertainty values and improved resolution due to finer grid spacing, a more accurate initial velocity model and less vertical smoothing. The 2D model also shows less vertical smearing than the 3D model, which may explain the very low sedimentary velocities obtained at the seafloor in the 3D model.

At shallow depths, the seafloor expression of the thrust ridges defines an area of comparatively lower velocities (< 1.7 km/s) (Fig. 11A, 12B) that extends to ~2 km beneath the sea surface (1 km below the seafloor) but with slightly increasing velocities due to sediment compaction (Fig. 12C). Many of these features are distributed over the ridges and the proximal intra-slope hemipelagic sedimentary basins that have been reported to be of biogenic origin, strongly diluted with high terrigenous input, mostly silty clays and clays (Flueh and Bialas, 2008) (Fig. 12C). There is also a spatial correlation between these zones and fluid activity inferred by heat flow anomalies, seafloor observations and sidescan mapping (Fig. 12).

Fig. 13A shows a seismic reflection line coincident with profile L10 that properly images the upper 500 m. A clear and continuous seafloor parallel reflection identified to be a gas hydrate-related bottom-simulating reflector (BSR), is mostly visible. However, several disruptions are observed and often coincide with dipping reflections, which might indicate a connection with the splay fault system mapped by Geersen et al., (2011) (Fig. 13B). The BSR indicates the base of the Gas Hydrate Stability Zone (GHSZ), which has a mean thickness of ~300 m along the profile. Because the BSR is caused by the impedance contrast between hydrate-bearing sediments and sediments containing free gas located right beneath it, it is a robust proxy for the presence of gas hydrate within the GHSZ (Tréhu et al., 2003). Although the corresponding free gas zone beneath the GHSZ should form a low velocity layer (Tréhu et al., 2001), this feature is not resolved by our models.

The near-surface velocity field within the GHSZ is not uniform along the profile (Fig. 13B). Even though V_p values lower than 1.7 km/s are predominant in the vicinity of the thrust ridges, there are two zones where the 2.0 km/s velocity contour is found above or close to the BSR (at ~30 km and at the north-eastern end of the profile; Fig. 13B). We speculate that decreasing V_p values within the GHSZ might indicate decreasing hydrate concentration. Tréhu et al. (2001; 2004a) suggested that free gas presence within the GHSZ may contribute to the local decrease in seismic velocity in the shallow sediment structure above the BSR. However, Tréhu et al, (2004b), discussed the potential mechanisms that allow free gas stability within the GHSZ and proposed that high gas saturation values may be the driving force for the focused flow to the GHSZ, that is, in focused conduits where free gas can be isolated from the pore water, hindering gas hydrate formation. Although there are no observable seismic indicators, such as bright spots above the BSR implying free gas conduits, (Fig. 13A), this situation cannot be ruled out considering evidence of effective gas migration through the GHSZ, as will be discussed later.

Reported advective fluid flow inferred by high heat flow anomalies is observed in the thrust ridge vicinity along profiles c728, ENAP-1 and VG06-74 in Figs. 12A and 12B (Grevemeyer et al., 2003; 2006; Villar-Muñoz et al., 2013). These results have been postulated as a geothermal evidence of the migration of warm fluids into the GHSZ through thrust faults that facilitate the vertical migration of fluids that originated at greater depth (Grevemeyer et al., 2006; Villar-Muñoz et al., 2013). Fig. 13D shows heat flow values derived from the BSR depths along profile L10, shown in Fig.13C (details of the calculations in the Supplementary material, section A3) and also includes the corresponding values of the previously discussed independent results at their intersection with this profile. The overall character of the results shows clear anomalies around fault-related reflectors for both the lithostatic and hydrostatic cases. Thus, we will only focus on the heat flows derived for the hydrostatic case, following the recommendation of Hyndman et al., (1992). Noteworthy shallowing of the BSR observed at 23 km and 38 km (Fig. 13C) results in high heat flow values (~40 mWm^{-2}; Fig. 11C) and are consistent with focused flow along thrust faults (Fig. 11B; Tréhu et al., 2003). The profile section between 28 and 39 km presents comparatively high heat flow rates (>35 mWm^{-2}) roughly consistent with the independent BSR-derived values (Fig. 11D) and above the theoretical thermal model at this distance from the deformation front reported by Grevemeyer et al., (2003) (~30 mWm^{-2} at ~40 km). Within this section, a gap between 30 and 32 km where no clear BSR is found coincides with a very high direct heat flow measurement (~120 mWm^{-2}; Grevemeyer et al., 2006) and a local uplift inferred by the calculated velocity structure and associated with lithological discontinuities (see velocity contours and inferred thrust faults in Fig. 13B).

410

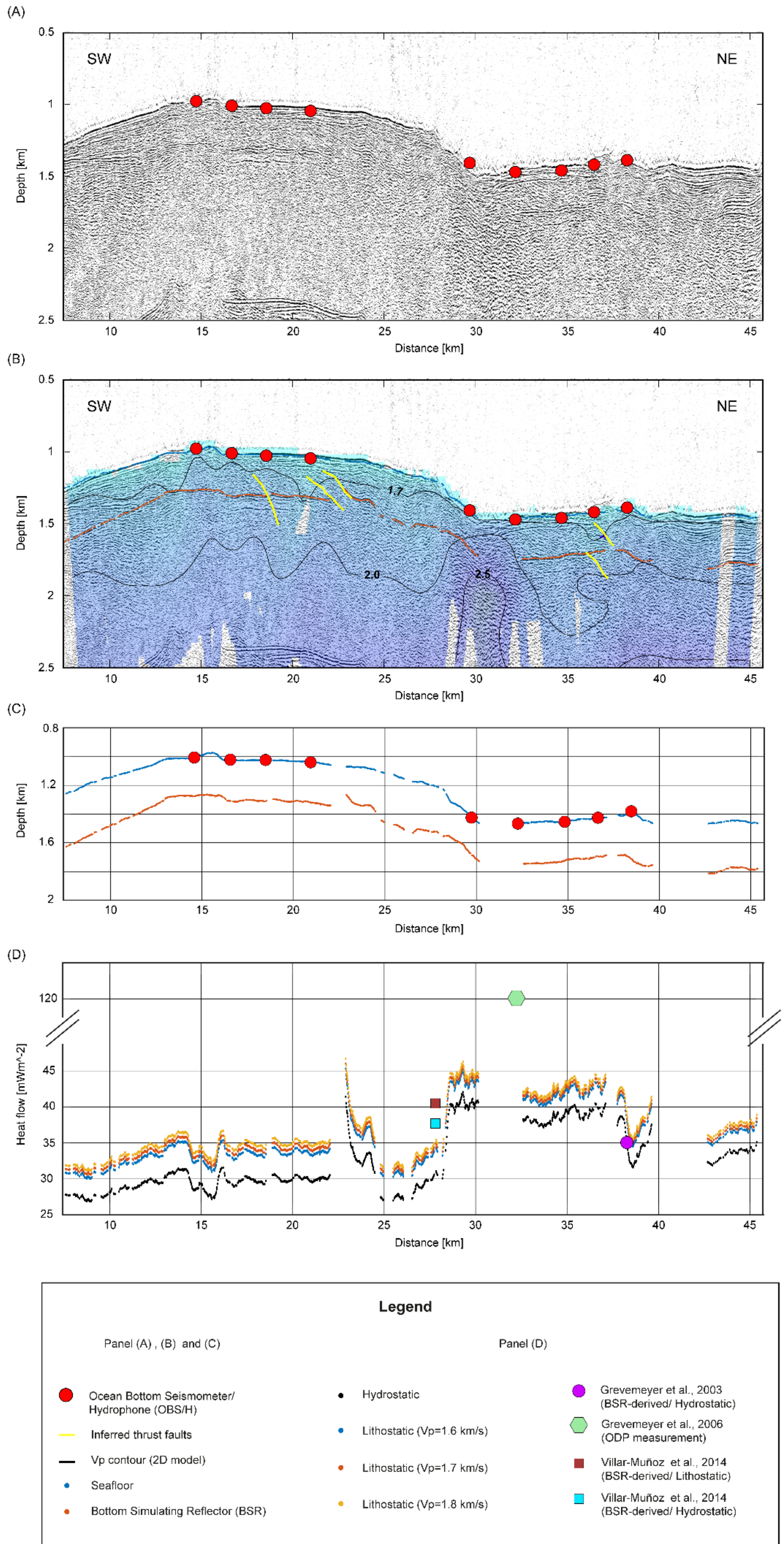
(A)
SW
NE
Depth [km]
Distance [km]
(B)
1.7
2.0
2.5
(C)
(D)
Heat flow [mWm^-2]
Legend
Panel (A) , (B) and (C)
Ocean Bottom Seismometer/ Hydrophone (OBS/H)
Inferred thrust faults
Vp contour (2D model)
Seafloor
Bottom Simulating Reflector (BSR)
Panel (D)
Hydrostatic
Lithostatic (Vp=1.6 km/s)
Lithostatic (Vp=1.7 km/s)
Lithostatic (Vp=1.8 km/s)
Grevemeyer et al., 2003 (BSR-derived/ Hydrostatic)
Grevemeyer et al., 2006 (ODP measurement)
Villar-Muñoz et al., 2014 (BSR-derived/ Lithostatic)
Villar-Muñoz et al., 2014 (BSR-derived/ Hydrostatic)

Fig. 13. (A) Depth-migrated seismic reflection coincident with profile L10. Conversion to depth was made using the 2D model shown in 11A. (B) Depth-migrated seismic reflection profile shown in (A), overlain by 2D velocity grid from Fig. 11A. Some velocity contours from the 2D model and instrument locations are overlain. The presence of BSR is indicated by red dots (also shown in (C)). Oblique reflections offsetting the BSR are interpreted as thrust faults (thick yellow lines). Thrust ridge location is visible as local seafloor uplift and distinctive reflection signature characterized by deformed sedimentary strata. In contrast, hemipelagic sediments in intra-slope basins are distinguished by predominantly parallel reflectors along a smoother seafloor. (C) Selection of seafloor and BSR reflections digitized from the seismic image in (A). Faint reflections and local disappearance of the BSR produce several gaps. Note disturbed BSRs around faults. (D) Heat flow values derived from BSR depths shown in (C) for a hydrostatic case and lithostatic case with different mean velocity values for the hydrate-bearing sediments. Different independent measurements coincident with profile L10 are overlain.

The presence of cold seeps has been documented by Klaucke et al., (2012) (Figs. 3 and 12). Seeps transport dissolved and gaseous compounds upward and sustain oasis-type ecosystems at the seafloor (Suess et al., 2018) such as the observed seep fauna comprising bacterial mats, shells of vesicolamyd clams (*Archivesica* sp) and large tubeworms of the *genus Lamellibrachia* (Klaucke et al., 2012) (Figs. 3 and 12). Moreover, methane related reactions -mainly AOM, anoxic oxidation of methane- involve consequent carbonate mineral precipitation near the seafloor (Suess et al., 2018), e.g., in the form of carbonate buildups (chemoherms), observed by Klaucke et al., (2012) (Figs. 3 and 12). As Suess et al. (2014) pointed out, cold seeps and their products have also been explained as the result of tectonic fluid expulsion by dewatering of sediments. Dewatering occurs in response to lateral compression by plate convergence and, as Cloos (1984) proposed, seafloor fluid flow through sediment facies may be explained by thrust faults acting as dewatering conduits. Landward of the accretionary wedge, splay faults developed in shallow angle subduction zones as off Cascadia, Japan and Southern Chile (as is the case of this study) are also proposed as drainage pathways of the upper plate (Moore et al., 2007).

Klaucke et al. (2012) reported little evidence of current seepage activity as e.g., gas flares or bubbles in the water column, suggesting either intense seepage in the past or moderate activity over prolonged periods of time. According to velocity-derived porosities for the upper 2.5 km (more details on the calculations are included in the Supplementary material, section A4), the low velocity sediments (< 1.7 km/s) that spatially correlate with these seep sites show high porosity values (> 50%). Therefore, as Bangs et al. (1990) proposed for the case of Barbados Accretionary complex, an overpressure caused by a considerable amount of pore fluids coming from underlying sediment facies as a result of a dewatering process, may also partially account for a decreasing seismic velocity in the shallow sediments.

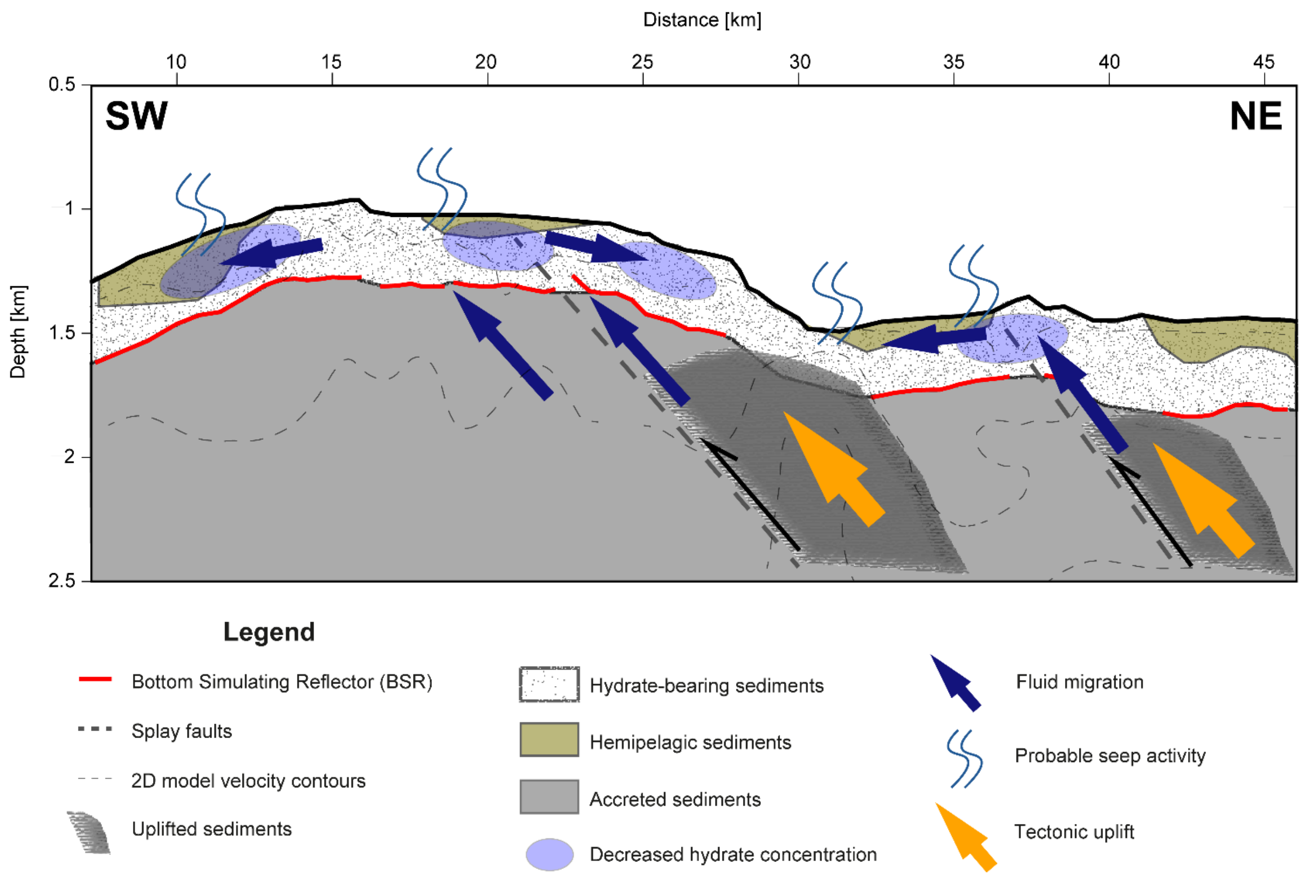

Fig. 14. Schematic interpretation of the study area based on the seismic structure along profile L10 in Fig. 13, summarizing the model results shown in Figs. 6-8, 11 and the tectonic interpretation in Fig. 12. Clusters of lower seismic velocity within the GHSZ (<1.7 km/s, see Fig. 13B) might be interpreted as hydrate-bearing sediments containing less hydrate concentration. Hemipelagic sediments in the intra-slope basins around the thrust ridges constitute the slope apron and are prone to experience seep activity (seepages, carbonate formations, seep biota). The interpreted accretionary prism is comprised between the 2.0 and 4.0 km/s; however, a transition zone composed of moderately porous accreted sediments (40-50% porosity) is present as noted by the region between the base of the GHSZ and the 2.0 km/s velocity contour (dotted grey line, see Fig. 13B for the velocity contour reference). This boundary also implies localized tectonic uplift associated with the splay faults. Fluid migration along these faults, represented by vertical blue arrows, may indicate the dewatering of the accretionary complex

implying a tectonically induced cold seep activity. Subsequent lateral fluid migration might also explain the existence of other adjacent reduced velocity zones within the GHSZ.

Accordingly, we propose that the observed seeps, evidenced by carbonate formations and seep biota at the seafloor are explained by the upward migration of methane-rich warm fluids into the high porosity sediments within the GHSZ, through splay faults associated with the thrust ridges (Fig. 14). Fluid flow through the gas hydrate stability field may occur where warm fluids move relatively quickly through permeable settings and keep the surrounding sediments warm enough to prevent gas hydrate formation (Grevemeyer et al., 2006). A differential hydrate concentration might be revealed by the variation of the near-surface velocity structure within the GHSZ, suggesting probable lateral fluid migration within the GHSZ along inclined sedimentary strata (Fig. 14).

On the other hand, at the NW region of the model, comparatively higher shallow velocities (>1.7 km/s), lower porosities (<50%) and higher velocity-depth gradients (~1.0 s^{-1}) are observed in areas of less disturbed seafloor, corresponding to parallel and horizontally stratified hemipelagic sediment sequences (Flueh and Bialas, 2008). This shallow behaviour is observed in seismic refraction profiles at these distances from the deformation front, outside the area of thrust ridges, as seen along P09 profile (see Fig. 2 for location). Even though resolution at the edge of the model decreases, extrapolation to seismic velocities observed in P09 (Contreras-Reyes et al., 2016) suggests that the increase in velocity is due mainly to the rock compaction processes unaffected by seepage activity.

5. Conclusions

A shallow 3-D P-wave tomography of the landward edge of the accretionary prism offshore SC Chile (35°- 36ºS) has been determined. Results show a primarily 2-D velocity distribution characterized by the presence of very low velocity zones within the GHSZ (<1.7 km/s), which are interpreted as highly porous sediments (higher than 50%) hosting less gas hydrate. A spatial correlation between these zones and evidence of seep activity (seep biota and BSR-derived heat flow anomalies as high as 40 Mwm^{-2}) in the vicinity of the locally NS trending thrust ridge indicate an increased supply of methane-rich fluids in the shallow sediments into the GHSZ. This situation responds to the existence of an accretionary complex experiencing a dewatering process due to overburden and tectonic stress.

Accretionary thrust ridges in this transition zone between the accretionary complex and the framework rock are the shallow expression of splay faults and are present in other accretionary margins such as the Nankai accretionary margin in Japan. In our study, these features are clear by their seafloor morphology signature and associated tectonic uplift has been inferred by increased lateral velocity gradients at depth. Thus, the dewatering of the accretionary complex is tectonically driven by these existing splay faults that act as fluid pathways for the draining of the upper plate.

The seismic velocity imaging of the upper sedimentary structure around thrust ridges can be a useful tool for the assessment of cold seep activity. However, better resolution needs to be achieved in order to characterize the GHSZ with more detail and additional seepage proxies are necessary for further insights into the relationship between shallow fluid activity in underconsolidated sediment deposits and their elastic properties such as V_p velocities.

6. Acknowledgments

We acknowledge the support of Programa de Investigación Asociativa (PIA): ANILLOS DE INVESTIGACION EN CIENCIA Y TECNOLOGÍA, CONICYT, grant ACT172002. This work was funded by CONICYT (Comisión Nacional de Ciencia y Tecnología) under the program Development of Research Projects between Chile and the United States CONICYT grant #USA2012–001. Cruise JC-23 with RRS JAMES COOK was carried out under the OFEG Barter agreement. Funds for JC-23 were granted by the German Science Foundation (DFG) through funding of the SFB-574 We would also like to thank Dr. Frauke Klingelhoefer and two anonymous reviewers, whose comments helped improve this manuscript.

7. Data availability

The research data used in this work is publicly available in an OSF repository (Obando-Orrego et al., 2020). It consists of SEG-Y files of each of the nine used instruments (hydrophone component) for the 5 seismic profiles (L10, L11, L12, L13, L14) and the corresponding navigation files (*ukooa* files). Also included are the corresponding migrated seismic reflection lines.

8. References

Adam, J., Klaeschen, D., Kukowski,N., Flueh, E., 2004. Upward delamination of Cascadia Basin sediment infill with landward frontal accretion thrusting caused by rapid glacial age material flux, Tectonics, 23, TC3009, doi:10.1029/2002TC001475.

Angermann, D., Klotz, J., Reigber, C., 1999. Space-geodetic estimation of the Nazca-South America Euler vector. Earth Planet Sci. Lett., 171(3):329–334.

Arsenault, M., Tréhu, A., Bangs, N., Nakamura, Y. 2001. P-wave Tomography of Hydrate Ridge, Oregon Continental Margin. EOS, Trans. Am. geophys. Un., 82(604), Abstract.

Bangs, N.L.B., Westbrook, G.K., Ladd, J.W., Buhl, P., 1990. Seismic velocities from the Barbados Ridge Complex: indicators of high pore fluid pressures in an accretionary complex. J. Geophys. Res.,95:8767−8782.

Bangs, N. L., Cande, S. C., 1997. Episodic development of a convergent margin inferred from structures and processes along the southern Chile margin. Tectonics, 16(3):486– 503, 1997.

Brown, K. M., Westbrook, G. K., 1987. The tectonic fabric of the Barbados Ridge Complex, Mar. Pet. Geol., 4, 71-81.

Brown, K. M., Westbrook, G. K., 1988. Mud diapirism and subcretion in the Barbados Ridge Complex, Tectonics, 7, 613–640.

Clift, P., Vannucchi, P., 2004. Controls on tectonic accretion versus erosion in subduction zones: implications for the origin and recycling on the continental crust. Reviews of Geophysics, 42.

Cloos, M., 1984. Landward-dipping reflectors in accretionary wedges: Active dewatering conduits? Geology, 12,519-522.

Contardo, X., Cembrano, J., Jensen, A., Diaz-Naveas, J., 2008. Tectono-sedimentary evolution of marine slope basins in the Chilean forearc (33°30′–36°50′S): Insights into their link with the subduction process. Tectonophysics. 206-218. 10.1016/j.tecto.2007.12.014.

Contreras-Reyes. E., Grevemeyer, I., Flueh, E. R., Scherwath M., Bialas, J., 2008**.** Effect of trench-outer rise bending-related faulting on seismic Poisson's ratio and mantle anisotropy: a case study offshore of southern central Chile, Geophys. J. Int., 173 (1), 142–156, doi:10.1111/j.1365-246X.2008.03716.x.

Contreras-Reyes E., Flueh, E. R., Grevemeyer, I., 2010. Tectonic control on sediment accretion and subduction off south-central chile: implications for coseismic rupture processes of the 1960 and 2010 megathrust earthquakes. Tectonics. doi.org/10.1029/2010TC002734.

Contreras-Reyes. E., Voelker, D., Bialas, J., Moscoso, E., Grevemeyer, I., 2016**.** Reloca Slide: an ~24 km³ submarine mass wasting event in response to over-steepening and failure of the central Chilean continental slope, Terra Nova ,28: 257-264, doi:10.1111/ter.12216.

Contreras-Reyes, E., Maksymowicz, A., Lange, D., Grevemeyer, I., Muñoz-Linford, P., Moscoso, E., 2017. On the relationship between structure, morphology and large coseismic slip: A case study of the Mw 8.8 Maule, Chile 2010 earthquake: Earth and Planetary Science Letters, v. 478, p. 27–39, https://doi.org/10.1016/j.epsl.2017.08.028.

Contreras-Reyes. E., 2018**.** Structure and Tectonics of the Chilean Convergent Margin from Wide-Angle Seismic Studies: A Review. In: Folguera A. et al. (eds) The Evolution of the Chilean-Argentinean Andes. Springer Earth System Sciences. Springer, Cham, p. 3–29, doi.org/10.1007/978-3-319-67774-3_1.

Díaz-Naveas, J. L., 1999. Sediment subduction and accretion at the Chilean convergent margin between 35°S and 40°S. Ph.D. dissertation.

Dickens,G.R., Quinby-Hunt, M.S. 1994. Methane hydrate stability in seawater. Geophys. Res Lett 21:2115–2118.

Farías, M., Comte, D., Roecker, S., Carrizo, D., Pardo, M., 2011. Crustal extensional faulting triggering by the 2010 Chilean earthquake: The Pichilemu seismic sequence. Tectonics, 30:TC6010.

Fisher, M.A., Flueh, E.R., Scholl, D.W., Parsons, T., Wells, R.E., Tréhu, A., ten Brink, U., Weaver, C.S., 1999. Geologic processes of accretion in the Cascadia subduction zone west of Washington state, Geodynamics, 27, 277-288.

Flueh, E., Bialas J., 2008. RRS JAMES COOK Cruise Report JC23-A & B, IFM-GEOMAR, Kiel. doi:10.329/ifm-geomar_rep_20_2008.

Geersen, J., Behrmann, J. H., Völker, D., Krastel, S., Ranero, C. R., Díaz-Naveas, J., Weinrebe, W., 2011. Active Tectonics of the South Central Chilean marine forearc (35◦S-40◦S). Tectonics, 30(TC3006).

Grevemeyer, I., Díaz-Naveas, C., Ranero, C. R., Villinger, H., Ocean Drilling Program Leg 202 Scientific Party., 2003. Heat flow over the descending Nazca plate in central Chile, 32°S to 41°S: Observations from ODP Leg 202 and the occurrence of natural gas hydrates. Earth Planet Sci. Lett., 213:285–298.

Grevemeyer, I., Kaul, N., Diaz-Naveas, J. L., 2006. Geothermal evidence for fluid flow through the gas hydrate stability field off Central Chile—transient flow related to large subduction zone earthquakes? Geophysical Journal International, Volume 166, Issue 1, Pages 461–468, https://doi.org/10.1111/j.1365-246X.2006.02940.x.

Hamilton, E. L. 1978. Sound velocity–density relations in sea- floor sediments and rocks. The Journal of the Acoustical Society of America, 63(2), 366–377.

Hornbach, M., Holbrook, S., Gorman, A., Hackwith, K., Lizarralde, D., Pecher, I., 2003. Direct seismic detection of methane hydrate on the Blake Ridge. Geophysics. 68. 10.1190/1.1543196.

Hyndman, R. D., Foucher, J. P., Yamano, M., Fisher, A., Scientific Team of Ocean Drilling Project leg 131, 1992. Deep sea bottom-simulating reflectors: Calibration of the base of the hydrate stability field as used for heat flow estimates. *Earth Planet. Sci. Lett.*, *109*, 289-301.

Hyndman, R. D., Moore, G. F., Moran, K., 1993. Velocity, porosity, and pore-fluid loss from the Nankai subduction zone accretionary prism, Proc. Integrated Ocean Drill. Program Sci. Results, 131, 211–220.

Hyndman, R.D., Spence, G.D., Yuan, T., Davis, E.E., 1994. Regional geophysics and structural framework of the Vancouver Island margin accretionary prisms, Proc ODP, Init. Rep., 146, 399-419.

Hyndman, R., Yorath, C., Clowes, R., Davis, E., 2011. The Northern Cascadia subduction zone at Vancouver Island—Seismic structure and tectonic history. Canadian Journal of Earth Sciences. 27. 313-329. 10.1139/e90-030.

Klaucke, I., Weinrebe, W., Linke, P., Kläschen, D., Bialas, J., 2012. Sidescan sonar imagery of widespread fossil and active cold seeps along the central Chilean continental margin. Geo-Mar Lett., 32:489.

Klaucke, I., Berndt, C., Crutchley, G., 2016. Fluid venting and seepage at accretionary ridges: The Four Way Closure Ridge offshore SW Taiwan. *Geo-Mar Lett* **36,** 165–174, https://doi.org/10.1007/s00367-015-0431-5.

Kopf, J., 2002. Significance of mud volcanism, Rev. Geophys., 40(2), 1005, doi:10.1029/2000RG000093.

Korenaga, J., Holbrook, W.S., Kent, G.M., Kelemen, P.B., Detrick, R.S., Larsen, H.C., Hopper, J.R., Dahl-Jensen, T., 2000. Crustal structure of the southeast Greenland margin from joint refraction and reflection seismic tomography. Journal of Geophysical Research, 105:21591–21614.

Kukowski, N., Oncken, O., 2006. Subduction Erosion — the “Normal” Mode of Fore-Arc Material Transfer along the Chilean Margin? 10.1007/978-3-540-48684-8_10.

Lange, D., Rietbrock, A., Haberland, C., Bataille, K., Dahm, T., Tilmann, F., Flueh, E. R., 2007. Seismicity and geometry of the south Chilean subduction zone (41,5 ◦S-43.5◦S): Implications for controlling parameters. Geophys. Res. Lett., 34, L06311:doi:10.1029/2006GL029190.

Lay, T., Ammon, C., Kanamori, H., Xue, L., Kim, M., 2011. Possible large near-trench slip during the 2011 Mw 9.0 off the Pacific coast of Tohoku Earthquake. Earth, Planets, and Space. 63. 10.5047/eps.2011.05.033.

Lieser, K., Grevemeyer, I., Lange, D., Flueh, E., Tilmann, F., Contreras-Reyes, E., 2014. Splay fault activity revealed by the aftershocks of the 2010 Mw 8.8 Maule earthquake, central Chile. Geological Society of America, 42(9):823–826.

Maksymowicz, A., Contreras-Reyes, E., Grevemeyer, I., Flueh, E., 2012. Structure and geodynamics of the post-collision zone between the Nazca–Antarctic spreading center and South America. Earth and Planetary Science Letters. s 345–348. 27–37. 10.1016/j.epsl.2012.06.023.

Maksymowicz, A., Chadwell, C. D., Ruiz, J., Tréhu, A. M., Contreras-Reyes. E., Weinrebe, W., Diaz-Naveas, J., Gibson, J. C., Lonsdale, P., Tryon, M. D., 2017. Coseismic seafloor deformation in the trench region during the Mw 8.8 Maule megathrust earthquake. Scientific Reports, 7:45918.

Melnick, D., Echtler H., 2006. Inversion of forearc basins in south- central Chile caused by rapid glacial age trench fill, Geology, 34(9), 709–712.

Moore, G., Shipley, T., Stoffa, P., Karig, D., Taira, A., Kuramoto, S., Tokuyama, H., Suyehiro, K., 1990. Structure of the Nankai Trough Accretionary Zone from multichannel seismic reflection data. Journal of Geophysical Research. 95. 8753-8766. 10.1029/JB095iB06p08753.

Moore, G. F., Bangs, N. L., Taira, A., Kuramoto, S., Pangborn, E., Tobin, H. J., 2007. Three-dimensional splay fault geometry and implications for tsunami generation. Science, 318(5853):1128–1131.

Moscoso, E., Grevemeyer, I., Contreras-Reyes, E., Flueh, E. R., Dzierma, Y., Rabbel, W., Thorwart, M., 2011. Revealing the deep structure and rupture plane of the 2010 Maule, Chile earthquake (Mw = 8.8) using wide angle seismic data. Earth Planet. Sci. Lett., 307:147–155.

[dataset] Obando-Orrego, S., Contreras-Reyes, E., Tréhu, A. M., Bialas, J., 2020. DATA: Shallow 3-D active-source P-wave velocity model of the accretionary complex offshore Central Chile. Electronic dataset, OSF Repository, doi:10.17605/OSF.IO/JDV54.

Olsen, K. M., Bangs, N. L., Tréhu, A. M., Han, S., Arnulf, A., Contreras-Reyes, E., 2020. Thick, strong sediment subduction along south-central Chile and its role in great earthquakes. Earth and Planetary Science Letters, 538, 116195. doi:10.1016/j.epsl.2020.116195.

Park, J. O., Tsuru T., Kodaira S., Cummins, P. R., Kaneda, Y., 2002. Splay fault branching along the Nankai subduction zone. Science 297:1157– 1160.

Ruiz, J., Hayes, G., Carrizo, D., Kanamori, H., Socquet, A., Comte, D., 2014. Seismological analyses of the 2010 March 11, Pichilemu, Chile M_w 7.0 and M_w 6.9 coastal intraplate earthquakes. Geophysical Journal International. 197.

Ryan, W.B.F., Carbotte, S.M., Coplan, J.O., O'Hara, S., Melkonian, A., Arko, R., Weissel, R.A., Ferrini, V., Goodwillie, A., Nitsche, F., Bonczkowski, J., Zemsky, R., 2009. Global Multi-Resolution Topography synthesis: Geochemistry Geophysics Geosystems, v. 10, Q03014, https://doi.org/10.1029/2008GC002332.

Scherwath, M., Contreras-Reyes, E., Flueh, R., Grevemeyer, I., Krabbenhoeft, A., Papenberg, C., Petersen, C. J., Weinrebe, R. W., 2009. Deep lithospheric structures along the southern central Chile margin from wide-angle P-wave modelling. Geophysics. J. Int., 179(1):579–600.

Schumann, K., Stipp, M., Behrmann, J. H., Klaeschen D., Schulte-Kortnack D., 2014. P and S wave velocity measurements of water-rich sediments from the Nankai Trough, Japan,J. Geophys. Res. Solid Earth, 119, 787–805, doi:10.1002/ 2013JB010290.

Suess, E., 2014. Marine cold seeps and their manifestations: geological control, biogeochemical criteria and environmental conditions. Intl J Earth Sci 103:1889–1916.

Suess, E., 2018. Marine Cold Seeps: Background and Recent Advances. 10.1007/978-3-319-54529-5_27-1.

Toomey, D. R., Solomon, S. C., Purdy, G. M., 1994. Tomographic imaging of the shallow crustal structure of the East Pacific Rise at 9° 30' N. J. Geophysics. Res., 99:24,135– 24,157.

Tréhu, A. M., Lin, G., Maxwell, E., Goldfinger, C., 1995. A seismic reflection profile across the Cascade subduction zone offshore central Oregon: new constraints on methane distribution and crustal structure, J. Geophys. Res., 100, 15,101-15,116.

Tréhu, A. M., Torres, M., Moore, G., Suess, E., Bohrmann, G., 1999. Dissociation of gas hydrates in response to slumping and folding on the Oregon continental margin, Geology, 27, 939-942.

Tréhu, A.M., Flueh, E., 2001. Estimating the thickness of the free gas zone beneath Hydrate Ridge, Oregon continental margin, from seismic velocities and attenuation. Journal of Geophysical Research. 106. 2035-2045. 10.1029/2000JB900390.

Tréhu, A.M., Stakes, D.S., Bartlett, C.D., Chevallier, J., Duncan, R.A., Goffredi, S.K., Potter, S.M., Salamy, K.A., 2003. Seismic and seafloor evidence for free gas, gas hydrates, and fluid seeps on the transform margin offshore Cape Mendocino, J. Geophys. Res., 108, 2263 (19 pp.), doi:10.1029/2001JB001679.

Tréhu, A.M., Flemings, P., Bangs, N., Chevallier, J., Gracia, E., Johnson, J., Riedel, M., C-S Liu, X., Riedel, M., Torres, M.E., 2004a. Feeding methane vents and gas hydrate deposits at south Hydrate Ridge, GRL, v. 31, L23310, doi:10.1029/2004GL021286.

Tréhu, A.M., Bohrman, G., Rack, F.R., Collett, T.S., Goldberg, D.S., Long, P.E., Milkov, A.V., Riedel, M., Schultheiss, P., Torres, M.E., Bangs, N.L., Barr, S.R., Borowski, W.S., Claypool, G.E., Delwiche, M.E., Dickens, G.R., Gracia, E., Guerin. G., Holland, M., Johnson, J.E., Lee, Y-J., Liu, C-S., Su, X., Teichert, B., Tomaru, H., Vanneste, M., Watanabe, M., Weinberger, J. L., 2004b. Three-dimensional distribution of gas hydrate beneath southern Hydrate Ridge: constraints from ODP Leg 204, Earth and Plan. Sci. Let, v. 222, p. 845-862, 2004.

Tréhu, A.M., Hass, B., de Moor, A., Maksymowicz, A., Contreras-Reyes, E., Vera, E., Tryon, M.D., 2019a. Geologic controls on up-dip and alongstrike propagation of slip during subduction zone earthquakes from a high-resolution seismic reflection survey across the northern limit of slip during the 2010 Mw 8.8 Maule earthquake, offshore Chile: Geosphere, v. 15, no. 6, p. 1751–1773, https://doi.org /10.1130/GES02099.1.

Tréhu, A.M., de Moor, A., Mieres Madrid, J., Sáez, M., Chadwell, C.D., Ortega-Culaciati, F., Ruiz, J., Ruiz, S., and Tryon, M.D., 2019b. Post-seismic response of the outer accretionary prism after the 2010 Maule earthquake, Chile: Geosphere, v. 16, no. X, p. 1–20, https://doi.org/10.1130/GES02102.1.

van Gool, J.A.M., Cawood, P.A., 1994. Frontal vs. basal accretion and contrasting particle paths in metamorphic thrust belts. Geology **22**:51–54.

Villar-Muñoz, L., Behrmann, J.H., Diaz-Naveas, J., 2014. Heat flow in the southern Chile forearc controlled by large-scale tectonic processes. Geo-Mar Lett **34,** 185–198. https://doi.org/10.1007/s00367-013-0353-z.

Völker, D., Geersen, J.M., Contreras-Reyes, E., Reichert, C., 2013. Sedimentary fill of the Chile Trench (32–46°S): Volumetric distribution and causal factors: Journal of the Geological Society, v. 170, p. 723–736, https://doi.org/10.1144/jgs2012-119.

Willner, A.P., 2005. Pressure-temperature evolution of a late Paleozoic paired metamorphic belt in north-central Chile (34°–35°30′S): Journal of Petrology, v. 46, p. 1805–1833, https://doi.org/10.1093/petrology/egi035.

Supplementary material

A1. Aftershock seismicity

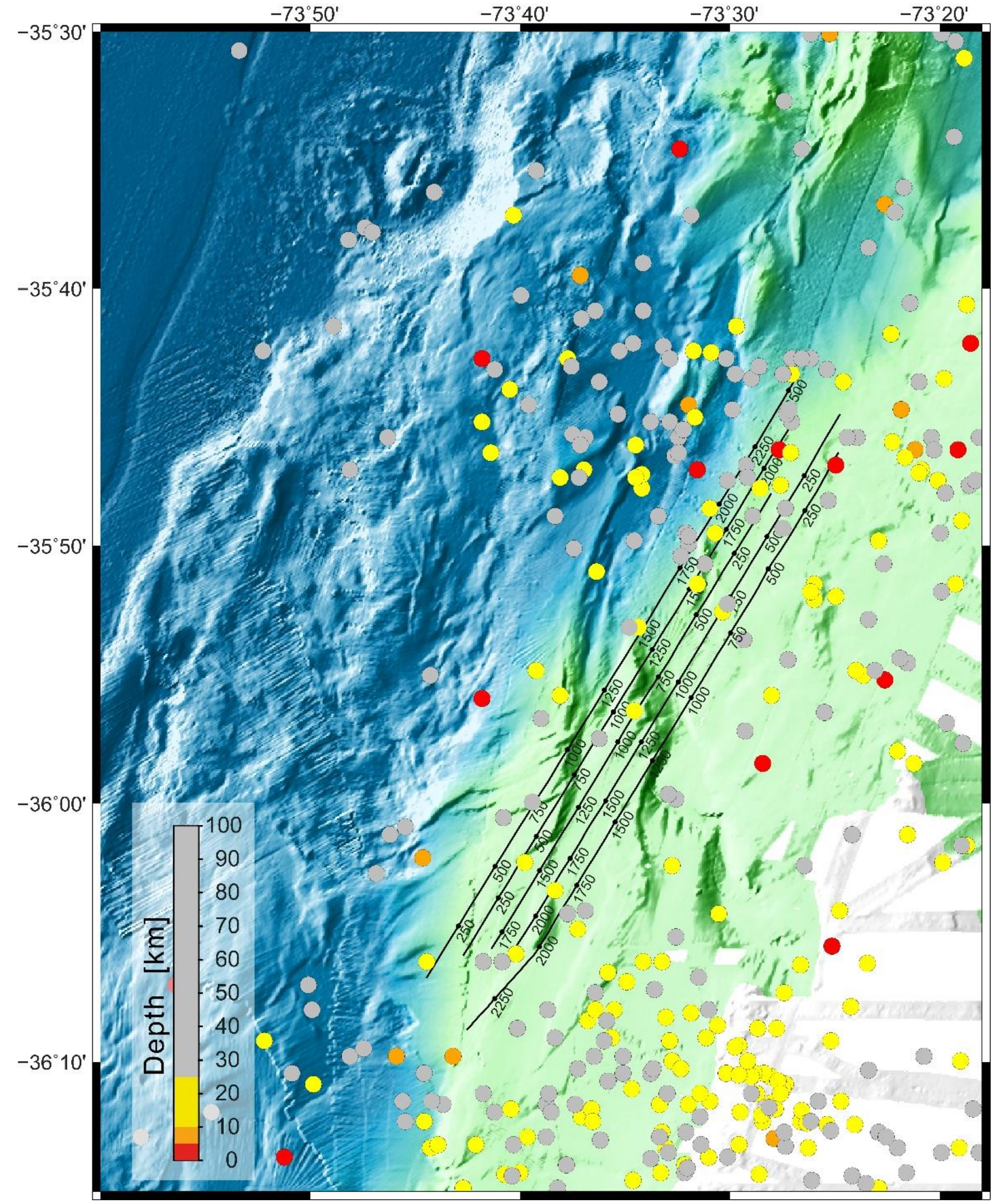

Supplementary Figure 1. Aftershock seismicity of the Maule earthquake depicted as circles color-coded by depth (Lange et al., 2012). Red and orange circles located around and trenchward from our study denote earthquakes occurring inside the accretionary prism. High-resolution bathymetric image of the seafloor off Maule region was collected during the RRS JAMES COOK cruise (Flueh and Bialas, 2008). Black lines correspond to the wide-angle seismic refraction profiles (L10, L11, L12, L13, L14) processed in this study whose gunshot locations are numbered every 250 shots (black dots along lines).

A2. 3D seismic records

The following figure shows examples of the seismic records from the instrument OBH 1002 along distal lines, that is, L11, L12, L13 and L14 lines (see Fig. 3 for profile locations).

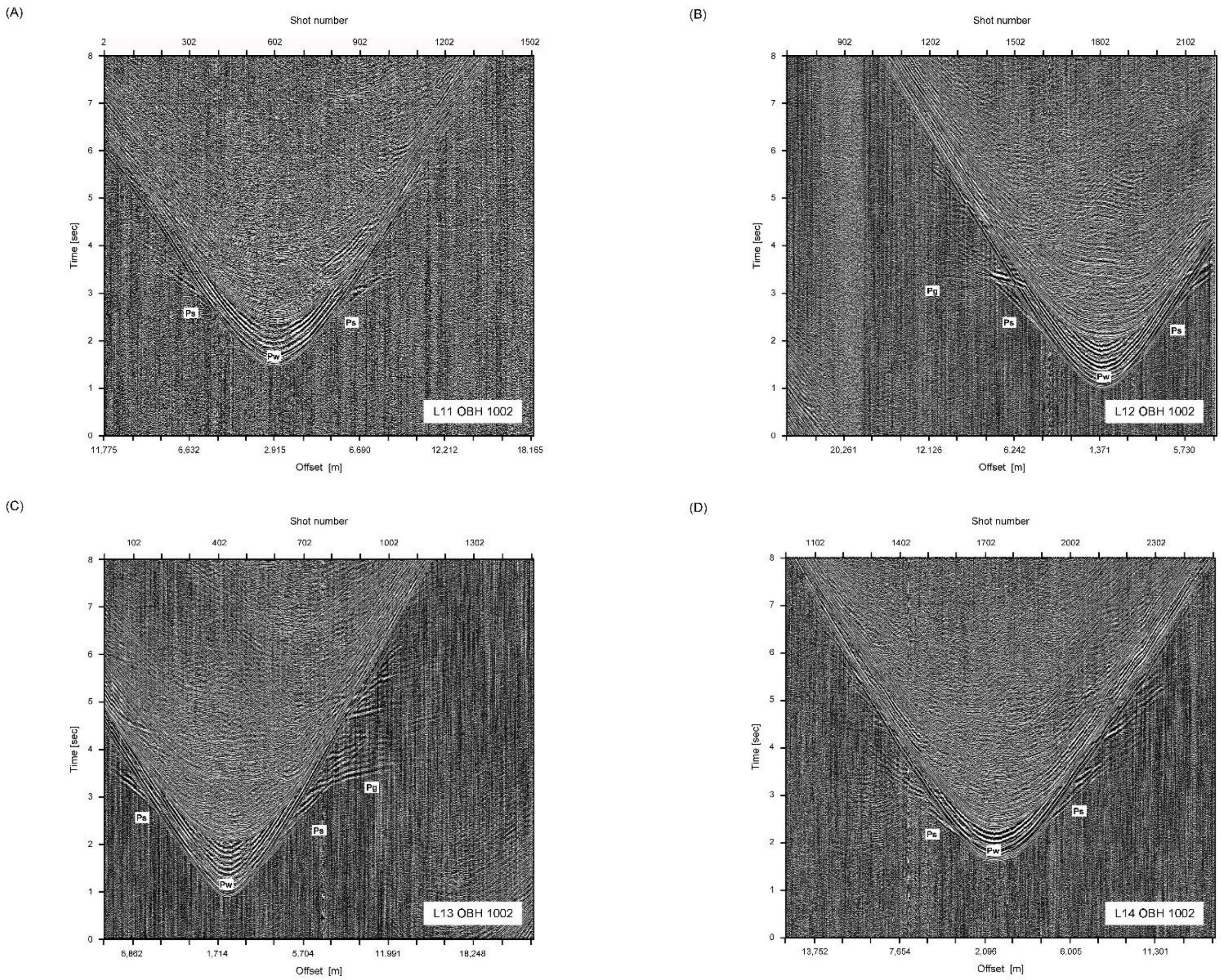

Supplementary Figure 2. Seismic records from instrument OBH 1002 along (A) L11, (B) L12, (C) L13, (D) L14 (see Fig. 3 in the main text for map reference). For each seismic record, the detected first-arriving P waves refractions are indicated: P_w (water wave arrival), P_s (low velocity sedimentary phase) and P_g (deeper sedimentary phases). Traces are ordered by shot number.

A3. Heat flow

Heat flow values along profile L10 derived by BSR depths, using a simple linear conductive heat relationship:

$$q = k (T_{BSR} - T_{seafloor}) / (Z_{BSR} – Z_{seafloor})$$

where q is the heat flow, k is the thermal conductivity, $T_{seafloor}$ is the temperature at the seafloor, T_{BSR} is the temperature at the BSR, Z_{BSR} and $Z_{seafloor}$ are depths of the BSR and seafloor, respectively. Thermal conductivity and seafloor temperature were obtained from Grevemeyer et al., (2003) based on ODP Leg 202 drillcore data (k=0.85 W/mK; $T_{seafloor}$=5°C). The BSR and the seafloor depths were obtained from the seismic profile shown in Fig. 11A. Z according to seismic profile. Temperature at BSR depth T_{BSR} is calculated using the dissociation temperature-pressure function T(p) of gas hydrates published by Dickens and Quinby-Hunt, (1994) for a seawater-methane system:

$$1/T = 3.79 \cdot 10^{-3} – 2.83 \cdot 10^{-4} \log(P)$$

where p is the pressure at the BSR (MPa) and T the temperature (Kelvin). Gas in the system is assumed to be pure methane, with a pore water salinity of 35 g l^{-1}. The pressure at BSR depth is studied for two cases: hydrostatic and lithostatic equilibrium. A density value for seawater of 1020 kg/m^3 was used and density for the sediment column were calculated using the relationship for soft sediments from Hamilton et al., (1978):

$$\rho = 1.135 V – 0.19$$

where V is velocity in km/s. We explored solutions for V= 1.6, 1.7 and 1.8 km/s for the hydrate-bearing sediments.

A4. Porosity values

In order to assess the degree of pore pressure in the shallow sediments, we calculated velocity-derived porosity values of the upper 2 km (Vp < 2.5 km/s). Empirical density-porosity and velocity-porosity relationships for characteristic deep-sea sediments have been derived by Hamilton (1978) and Hyndman et al., (1993), respectively. Hyndman's relation was derived from laboratory experiments of marine sediments in the Nankai accretionary margin, Japan, and by first approximation, was applied here in the valid range of porosities of 30-60% (~1600 and 2500 m/s). According to this relation,

(1) $$P = -1.180 + 8.607\,(1/V) - 17.89\,(1/V)^2 + 13.94\,(1/V)^3$$

where P is porosity (%) and V is velocity in km/s.

Alternatively, we computed densities from seismic velocities using Hamilton's relation derived from carbonate silt clays, turbidites, mudstones, and shales forming the soft and unlithified upper 500 m sediment layers, which is valid in the approximate range of 1.53-2.0 km/s:

(2) $$\rho = 1.135\,V - 0.19,$$

where V is the P-wave velocity (km/s) and ρ is density in g/cm^3. Porosity values were then derived using the corresponding definition:

(3) $$P = 100\,((\rho - \rho_m) / (\rho_f - \rho_m)),$$

where P is porosity (%), ρ is density (g/cm3), ρ_f corresponds to seawater density of 1.020 g/cm3 and ρ_m is the grain density. We used a value of 2.7 g/cm^3 corresponding to silica.

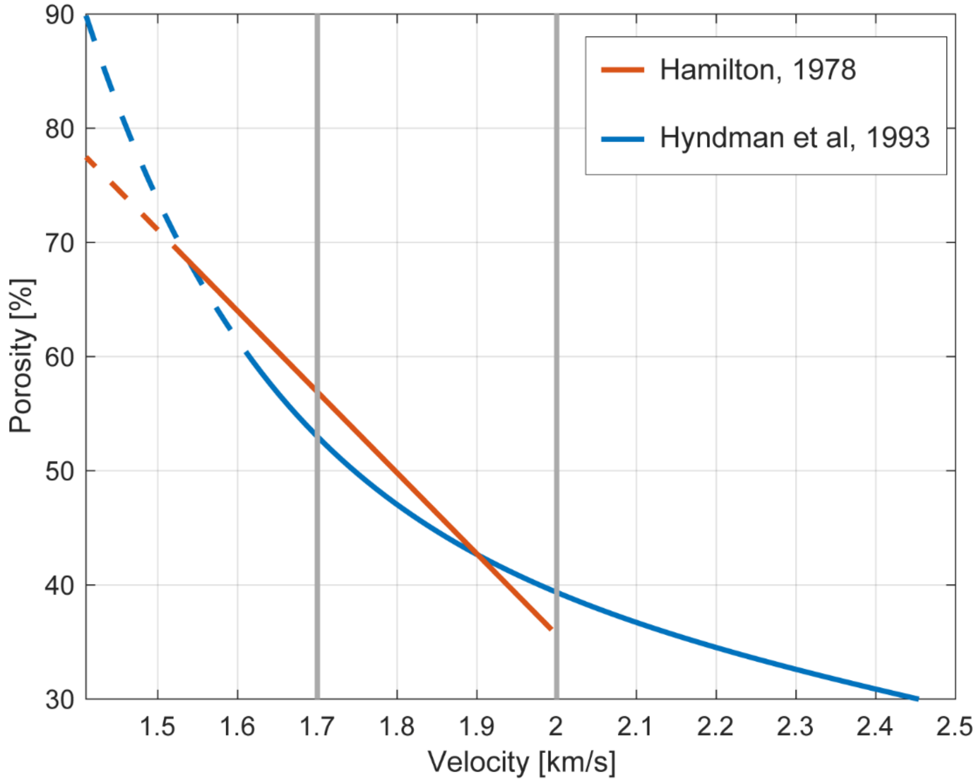

Supplementary Figure 3. Porosity versus velocity using Hamilton and Hyndman relations. Dashed sections of the curves indicate extrapolation of the porosity values outside the respective valid ranges. Accordingly, velocities lower than 1.53 km/s might imply porosities higher than 70%.

Figure

Click here to access/download;Figure;Fig.1.tif

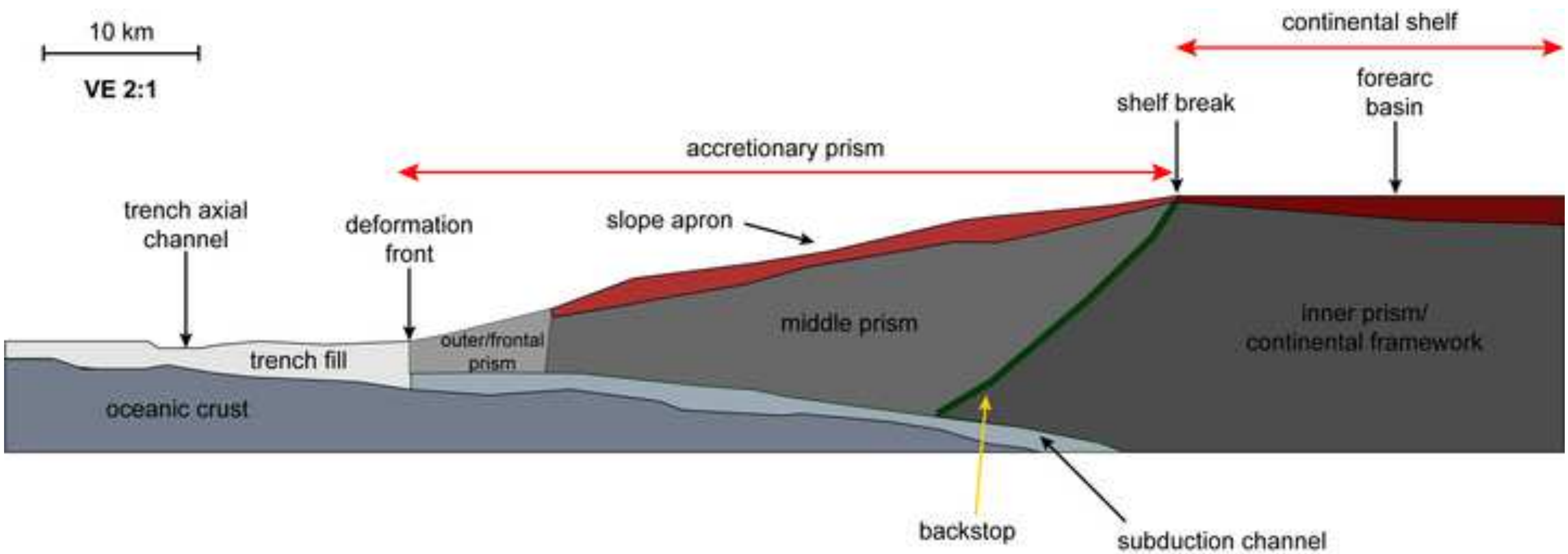

Figure

Click here to access/download;Figure;Fig.2.tif

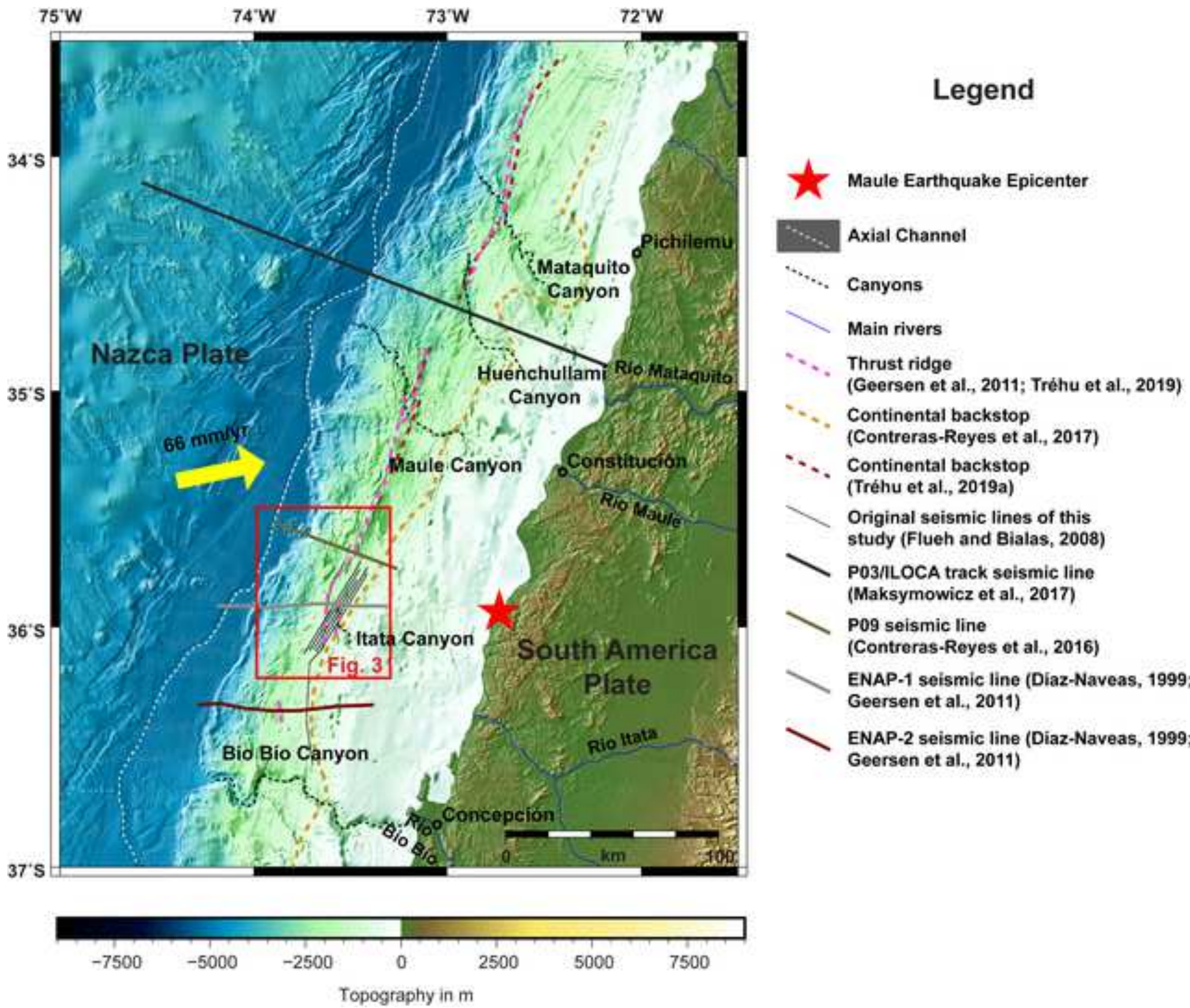

Figure

Click here to access/download;Figure;Fig.3.tif

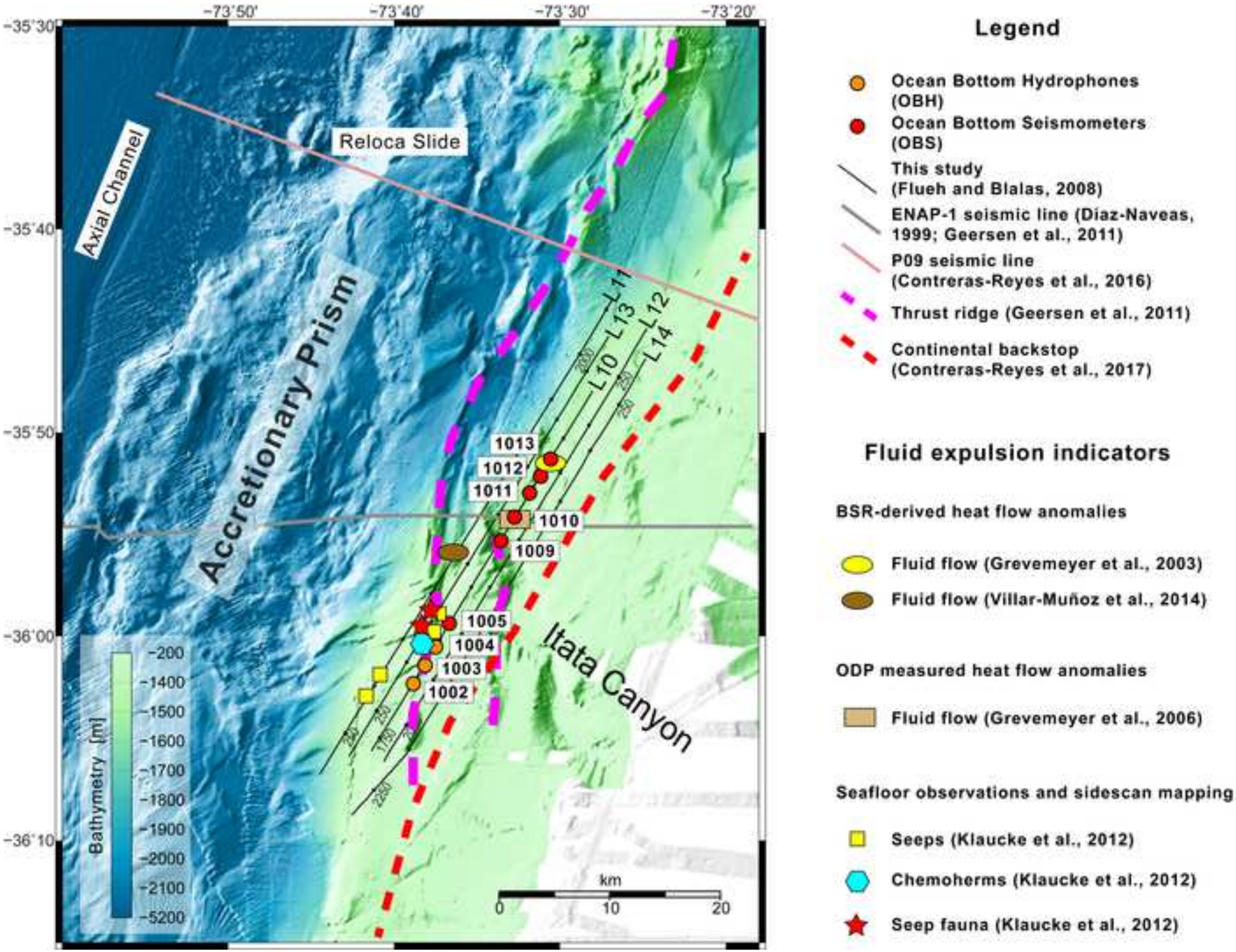

Figure

Click here to access/download;Figure;Fig.4.tif

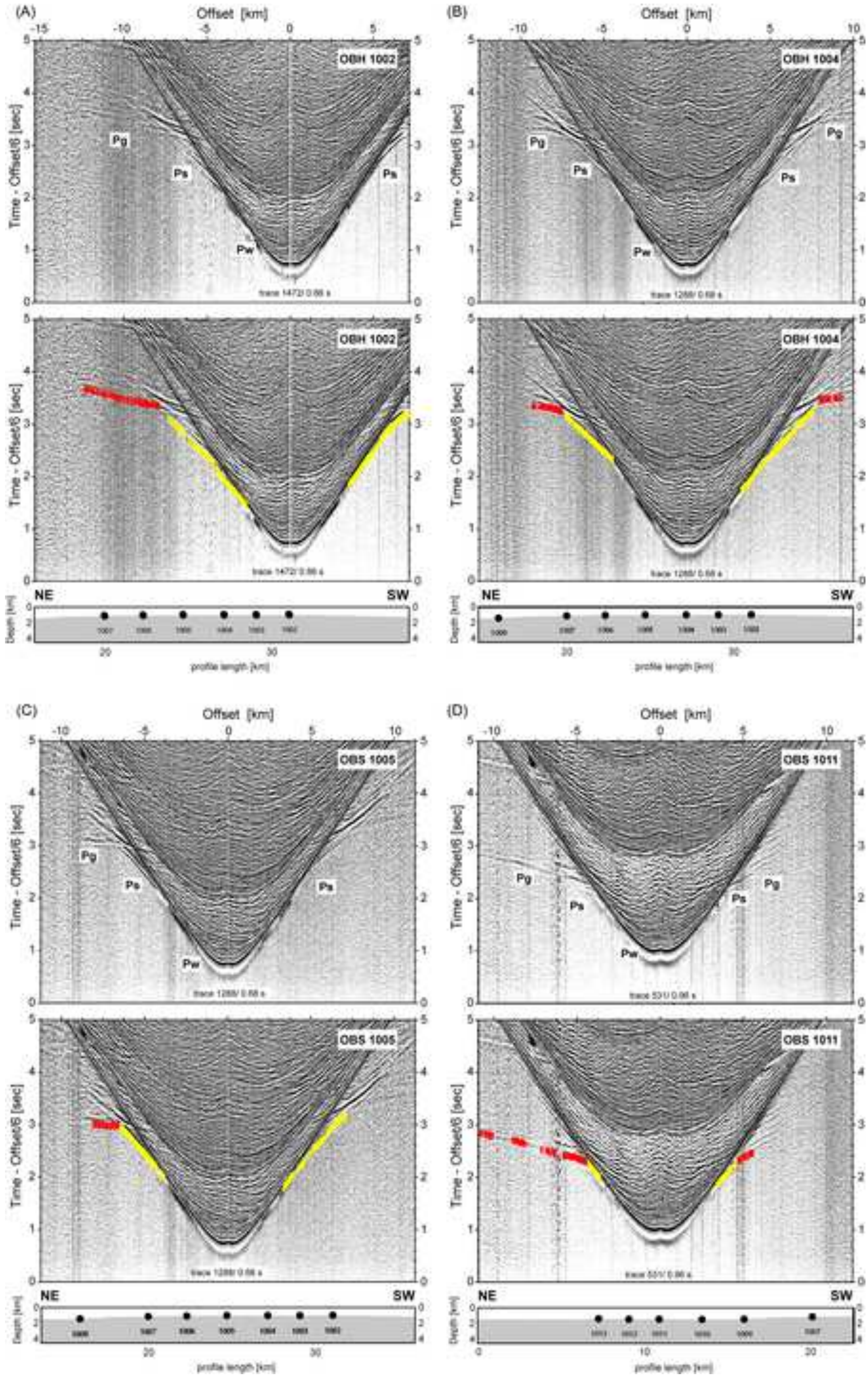

Figure

Click here to access/download;Figure;Fig.5.tif

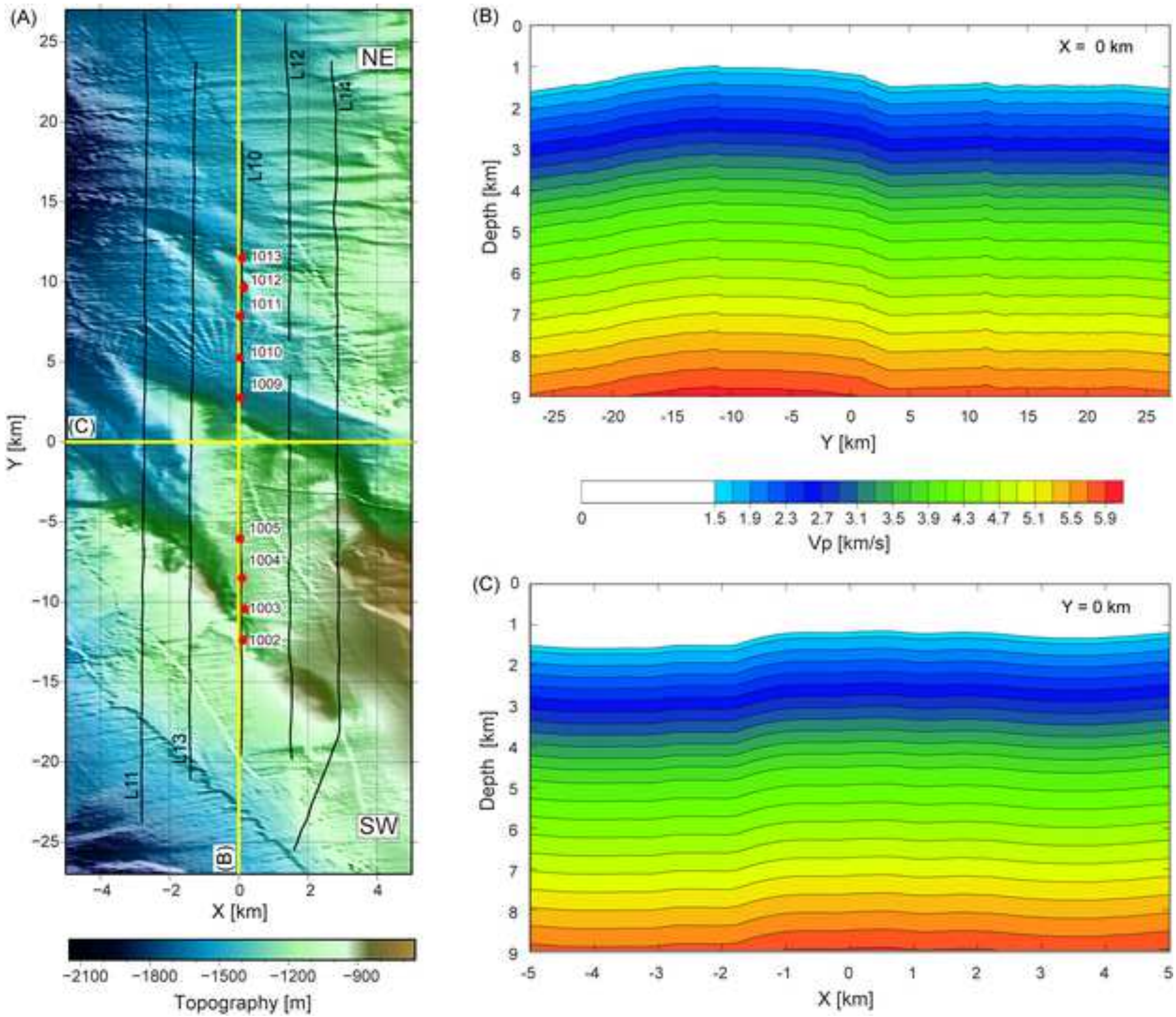

Figure

Click here to access/download;Figure;Fig.6.tif

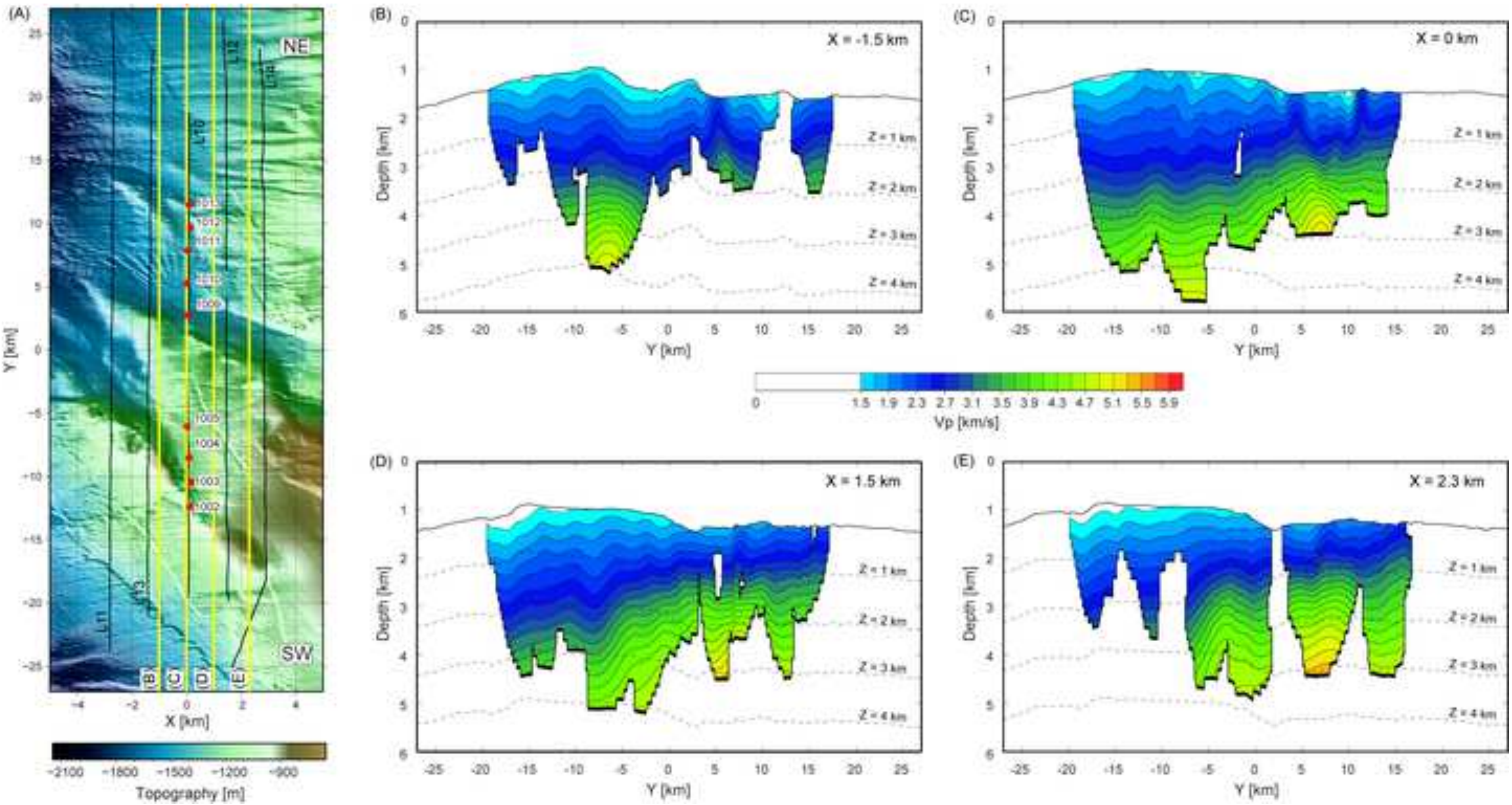

Figure

Click here to access/download;Figure;Fig.7.tif

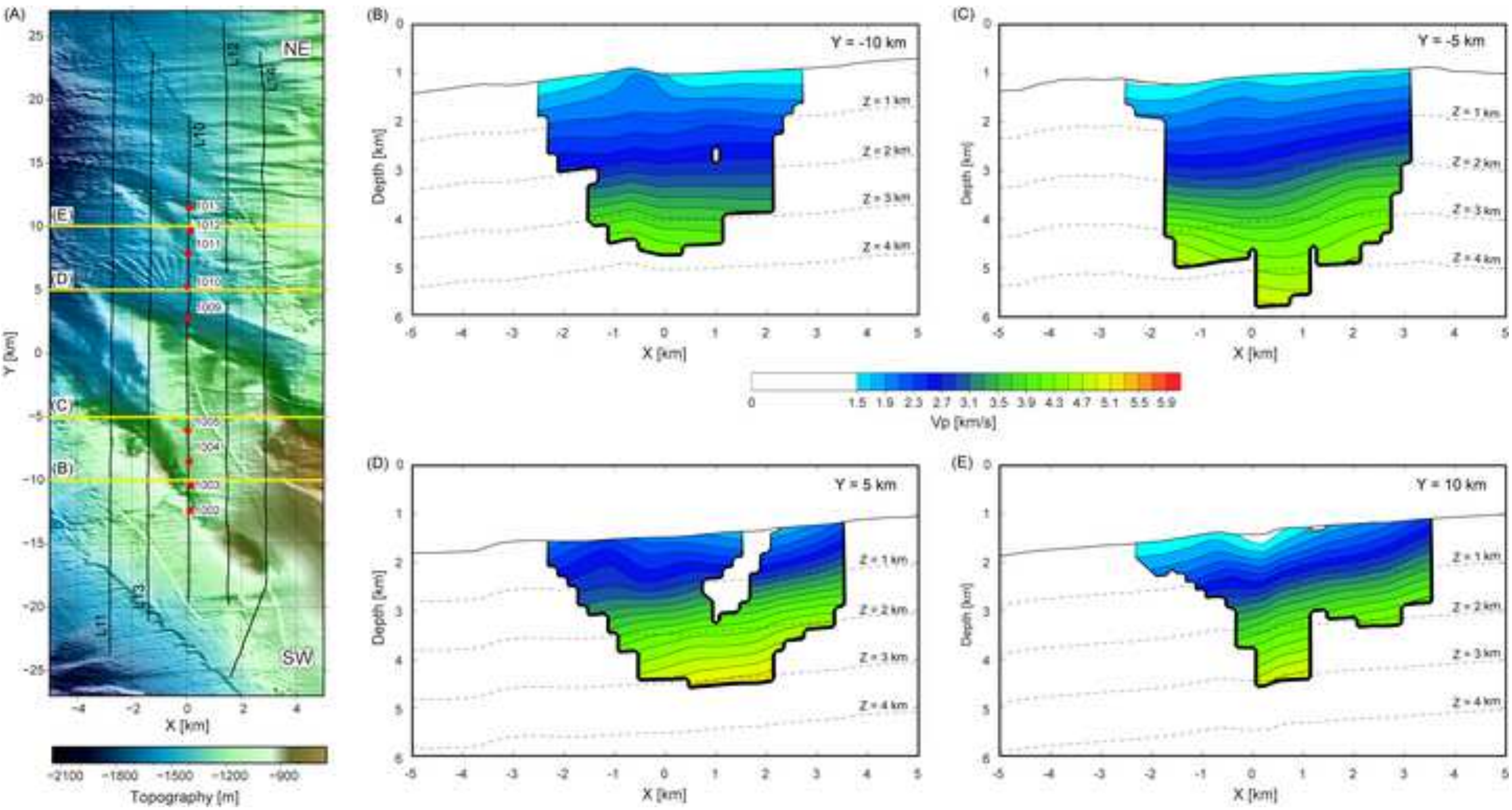

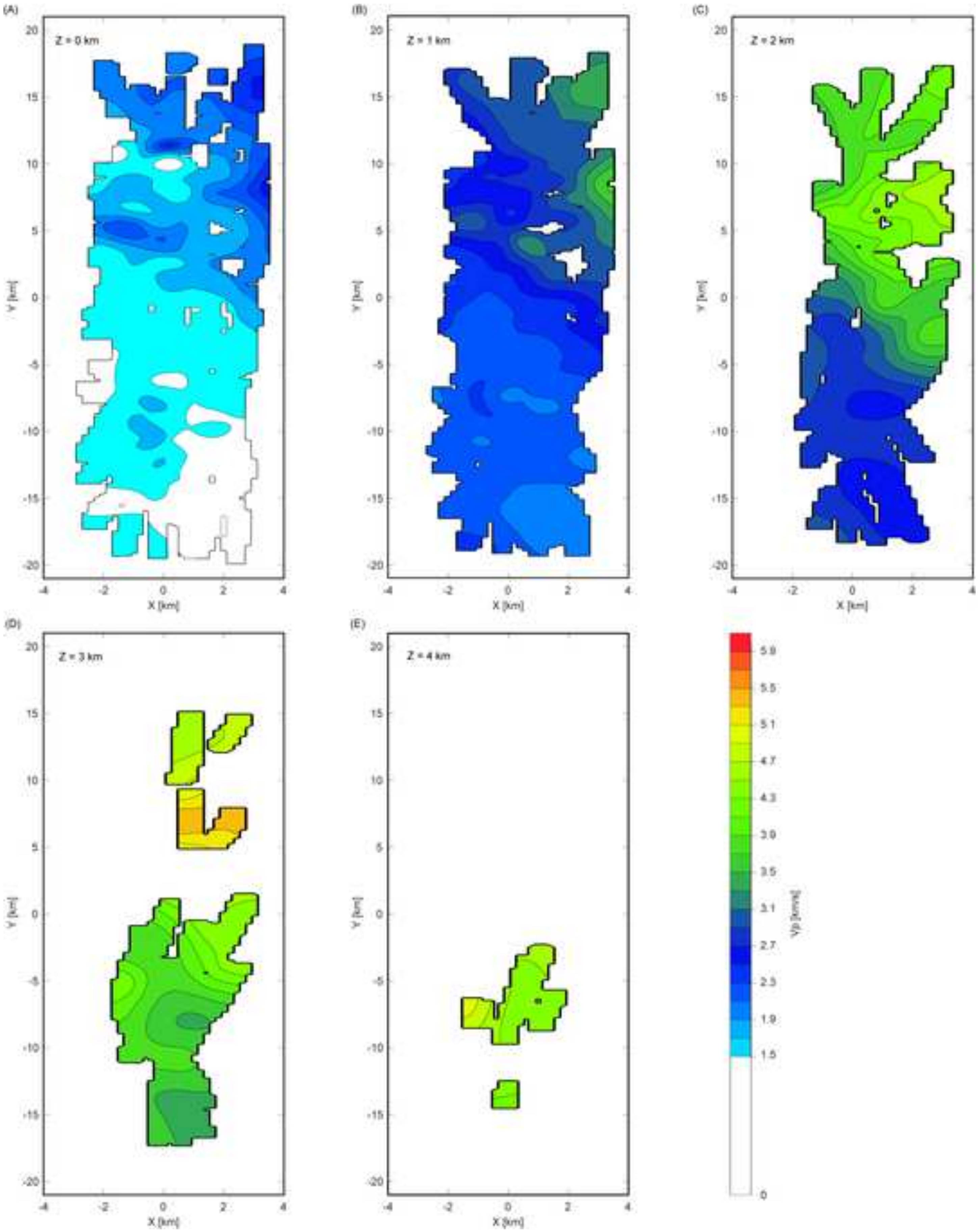
(A)
Z = 0 km
(B)
Z = 1 km
(C)
Z = 2 km
(D)
Z = 3 km
(E)
Z = 4 km
Y [km]
X [km]
Vp [km/s]
5.9
5.5
5.1
4.7
4.3
3.9
3.5
3.1
2.7
2.3
1.9
1.5
0

Figure

Click here to access/download;Figure;Fig.9.tif

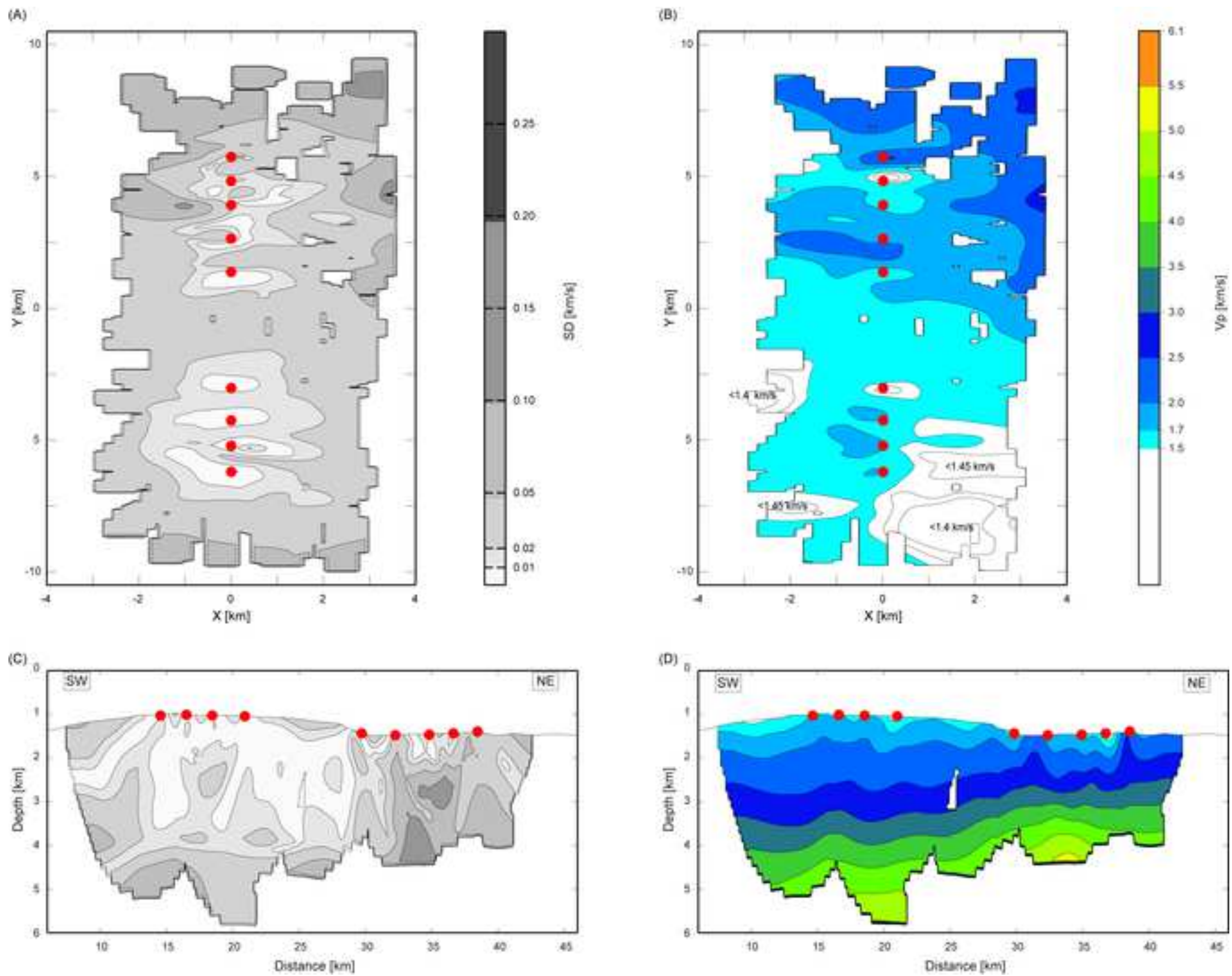

Figure

Click here to access/download;Figure;Fig.10.tif

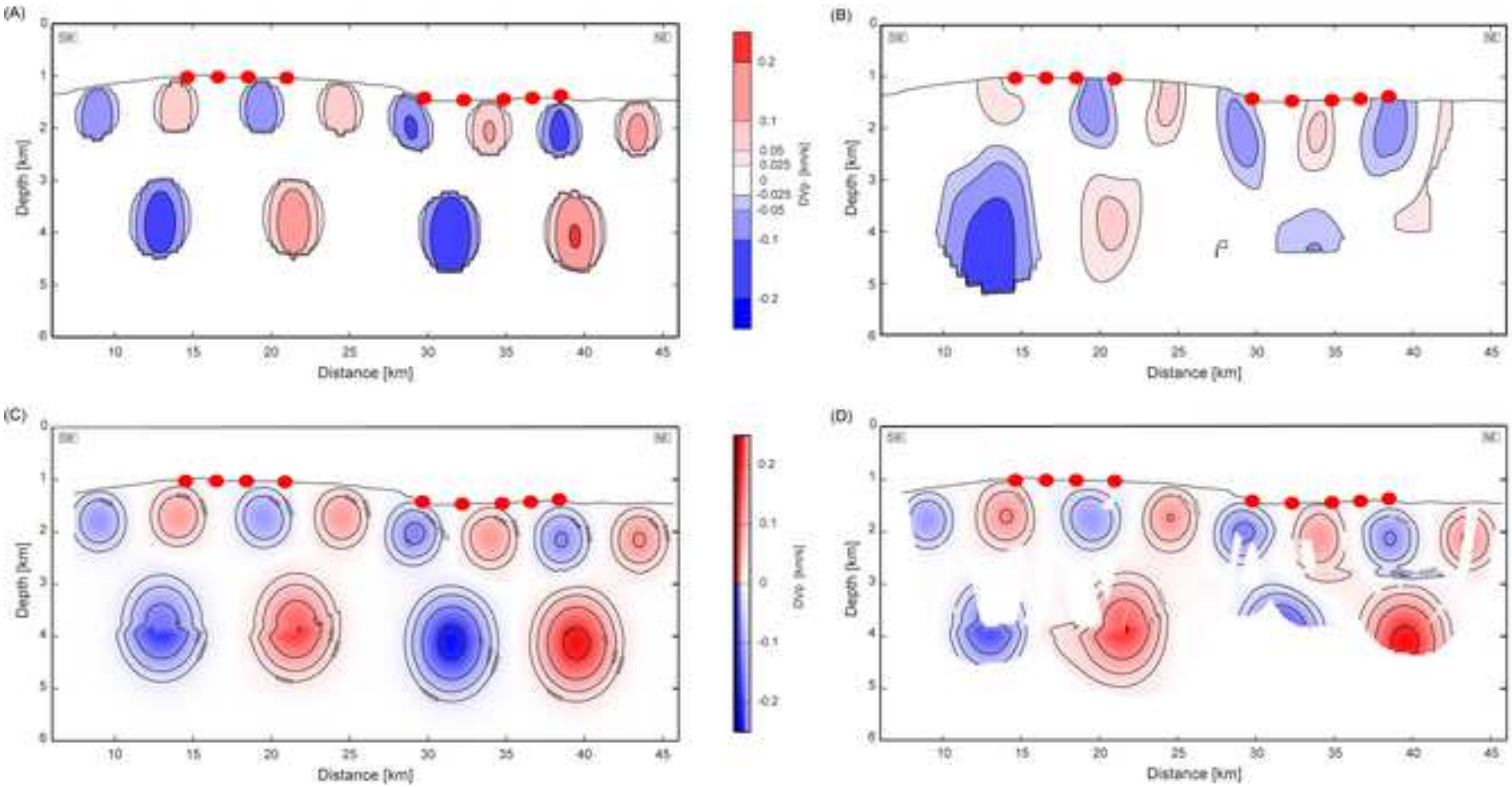

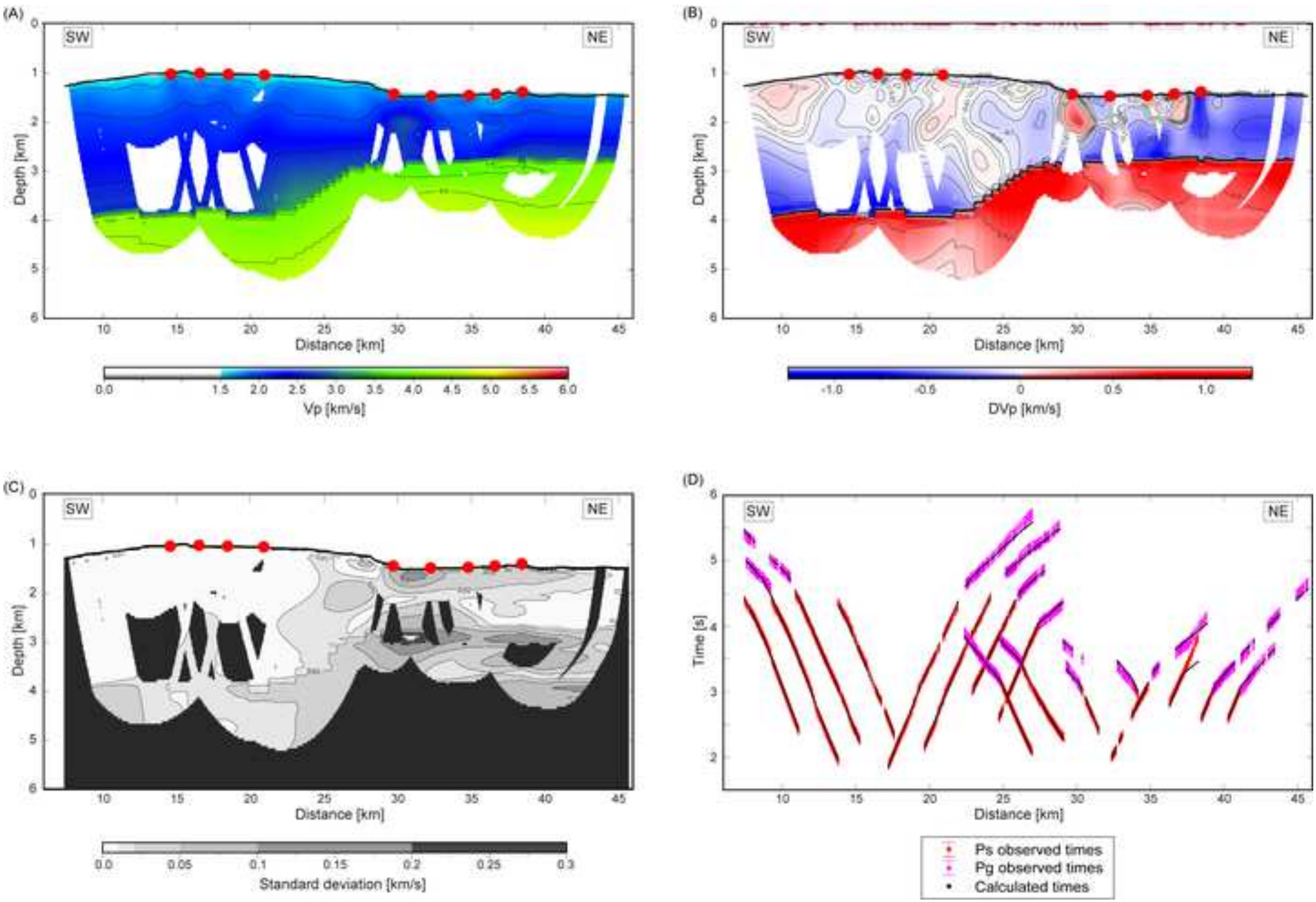
(A)
SW
NE
Depth [km]
Distance [km]
Vp [km/s]
0.0 1.5 2.0 2.5 3.0 3.5 4.0 4.5 5.0 5.5 6.0
(B)
DVp [km/s]
-1.0 -0.5 0 0.5 1.0
(C)
Standard deviation [km/s]
0.0 0.05 0.1 0.15 0.2 0.25 0.3
(D)
Time [s]
Ps observed times
Pg observed times
Calculated times

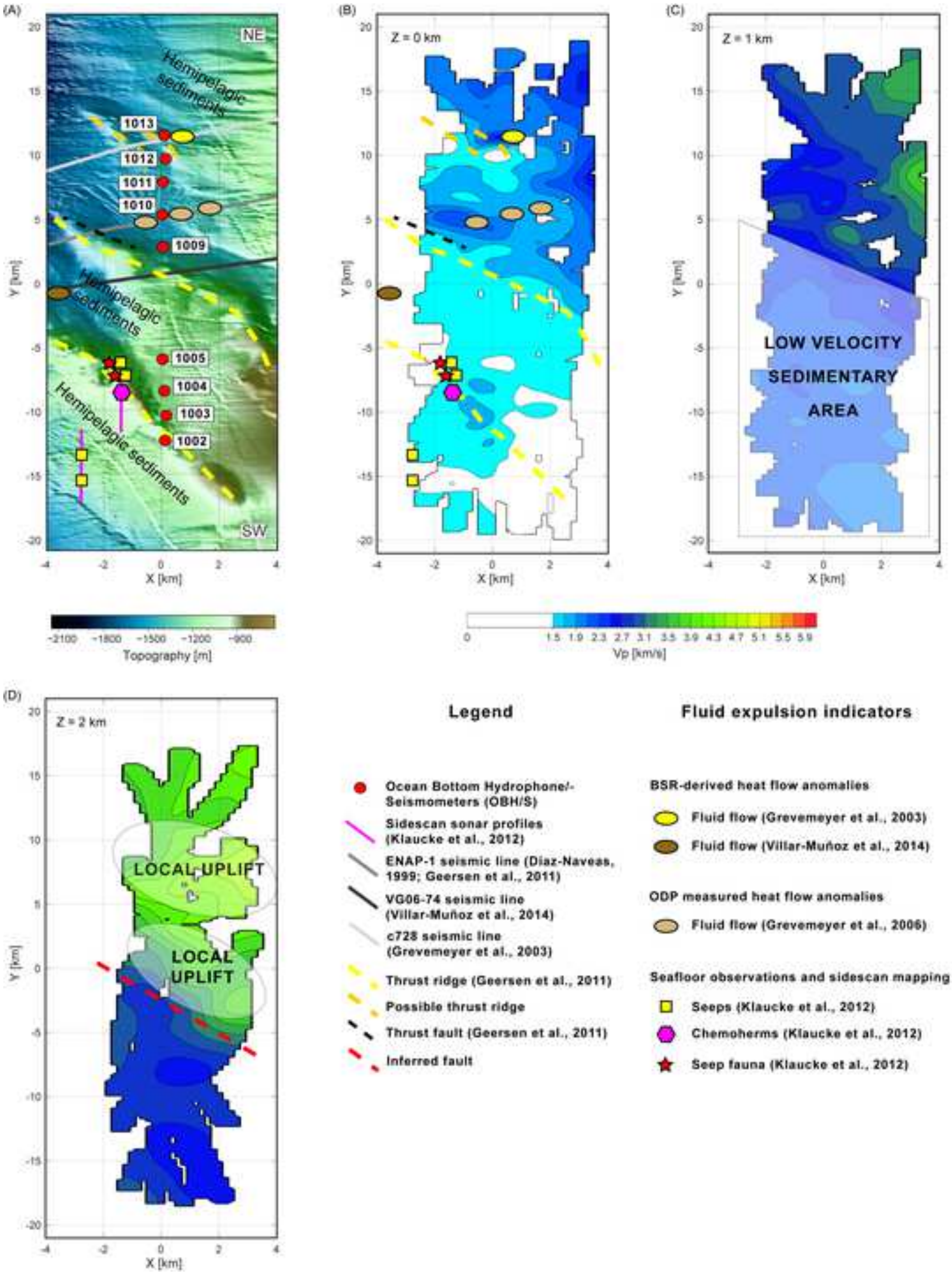
(A)
NE
SW
Hemipelagic sediments
Hemipelagic sediments
Hemipelagic sediments
1013
1012
1011
1010
1009
1005
1004
1003
1002
Y [km]
X [km]
Topography [m]
-2100
-1800
-1500
-1200
-900
(B)
Z = 0 km
(C)
Z = 1 km
LOW VELOCITY SEDIMENTARY AREA
Vp [km/s]
0
1.5
1.9
2.3
2.7
3.1
3.5
3.9
4.3
4.7
5.1
5.5
5.9
(D)
Z = 2 km
LOCAL UPLIFT
LOCAL UPLIFT
Legend
Ocean Bottom Hydrophone/-Seismometers (OBH/S)
Sidescan sonar profiles (Klaucke et al., 2012)
ENAP-1 seismic line (Díaz-Naveas, 1999; Geersen et al., 2011)
VG06-74 seismic line (Villar-Muñoz et al., 2014)
c728 seismic line (Grevemeyer et al., 2003)
Thrust ridge (Geersen et al., 2011)
Possible thrust ridge
Thrust fault (Geersen et al., 2011)
Inferred fault
Fluid expulsion indicators
BSR-derived heat flow anomalies
Fluid flow (Grevemeyer et al., 2003)
Fluid flow (Villar-Muñoz et al., 2014)
ODP measured heat flow anomalies
Fluid flow (Grevemeyer et al., 2006)
Seafloor observations and sidescan mapping
Seeps (Klaucke et al., 2012)
Chemoherms (Klaucke et al., 2012)
Seep fauna (Klaucke et al., 2012)

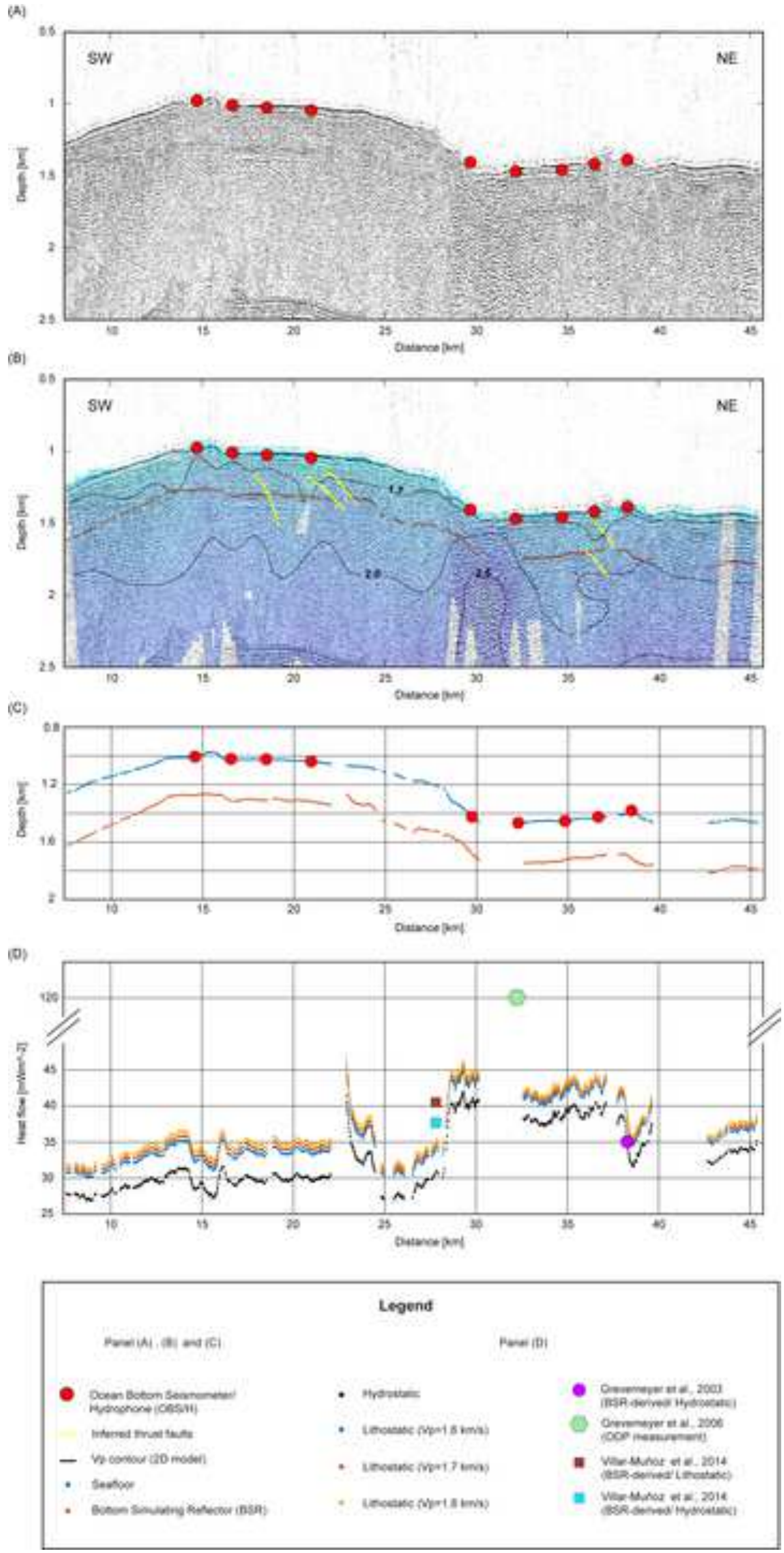
(A)
SW
NE
Depth [km]
Distance [km]
(B)
SW
NE
1.7
2.0
2.5
Depth [km]
Distance [km]
(C)
Depth [km]
Distance [km]
(D)
Heat flow [mW/m^2]
Distance [km]
Legend
Panel (A), (B) and (C)
Panel (D)
Ocean Bottom Seismometer/ Hydrophone (OBS/H)
Inferred thrust faults
Vp contour (2D model)
Seafloor
Bottom Simulating Reflector (BSR)
Hydrostatic
Lithostatic (Vp=1.6 km/s)
Lithostatic (Vp=1.7 km/s)
Lithostatic (Vp=1.8 km/s)
Grevemeyer et al., 2003 (BSR-derived/ Hydrostatic)
Grevemeyer et al., 2006 (ODP measurement)
Villar-Muñoz et al., 2014 (BSR-derived/ Lithostatic)
Villar-Muñoz et al., 2014 (BSR-derived/ Hydrostatic)

Figure

Click here to access/download;Figure;Fig.14.tif

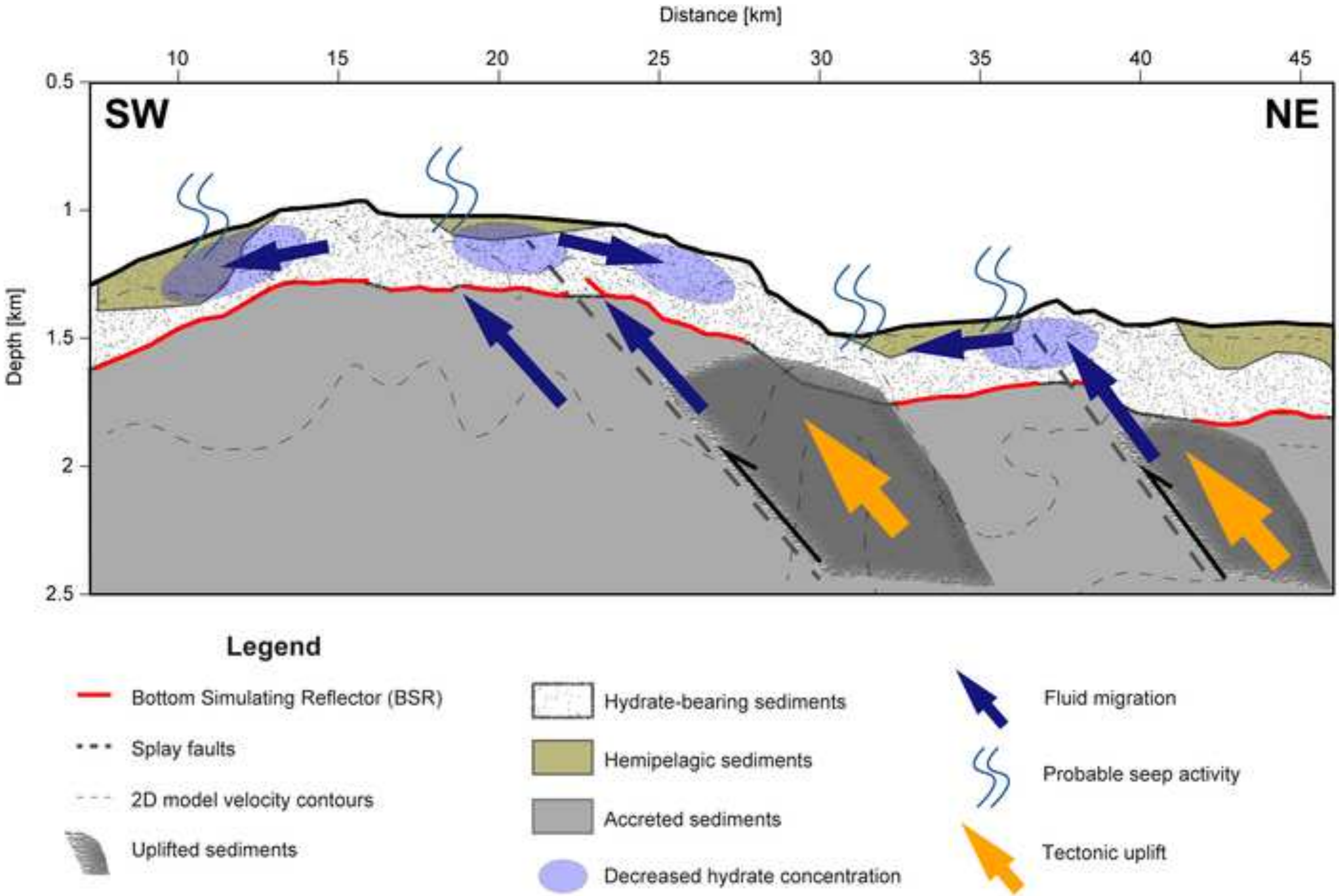

Figure

Click here to access/download;Figure;Supplementary_Fig.1.tif

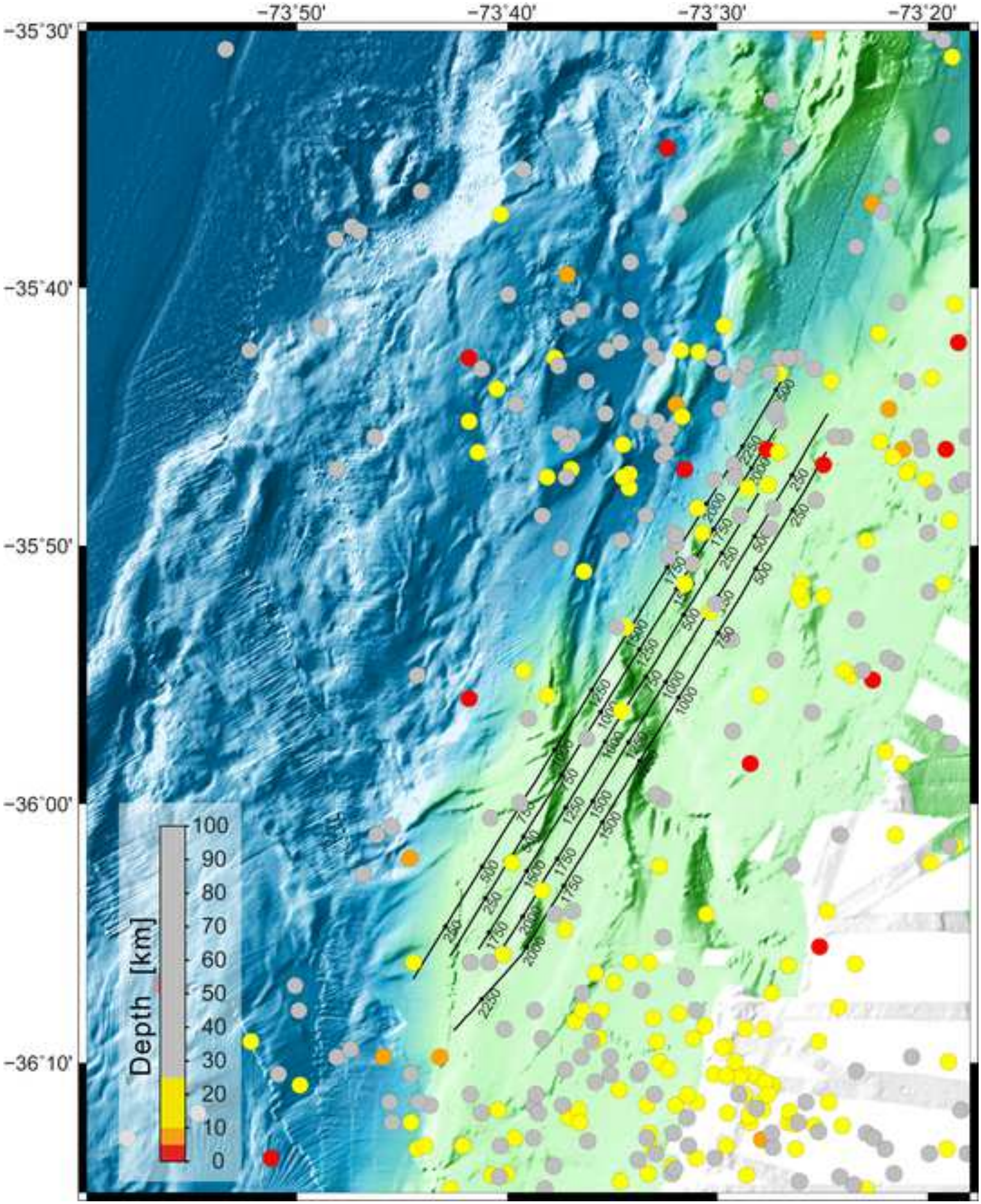

Figure

Click here to access/download;Figure;Supplementary_Fig.2.tif

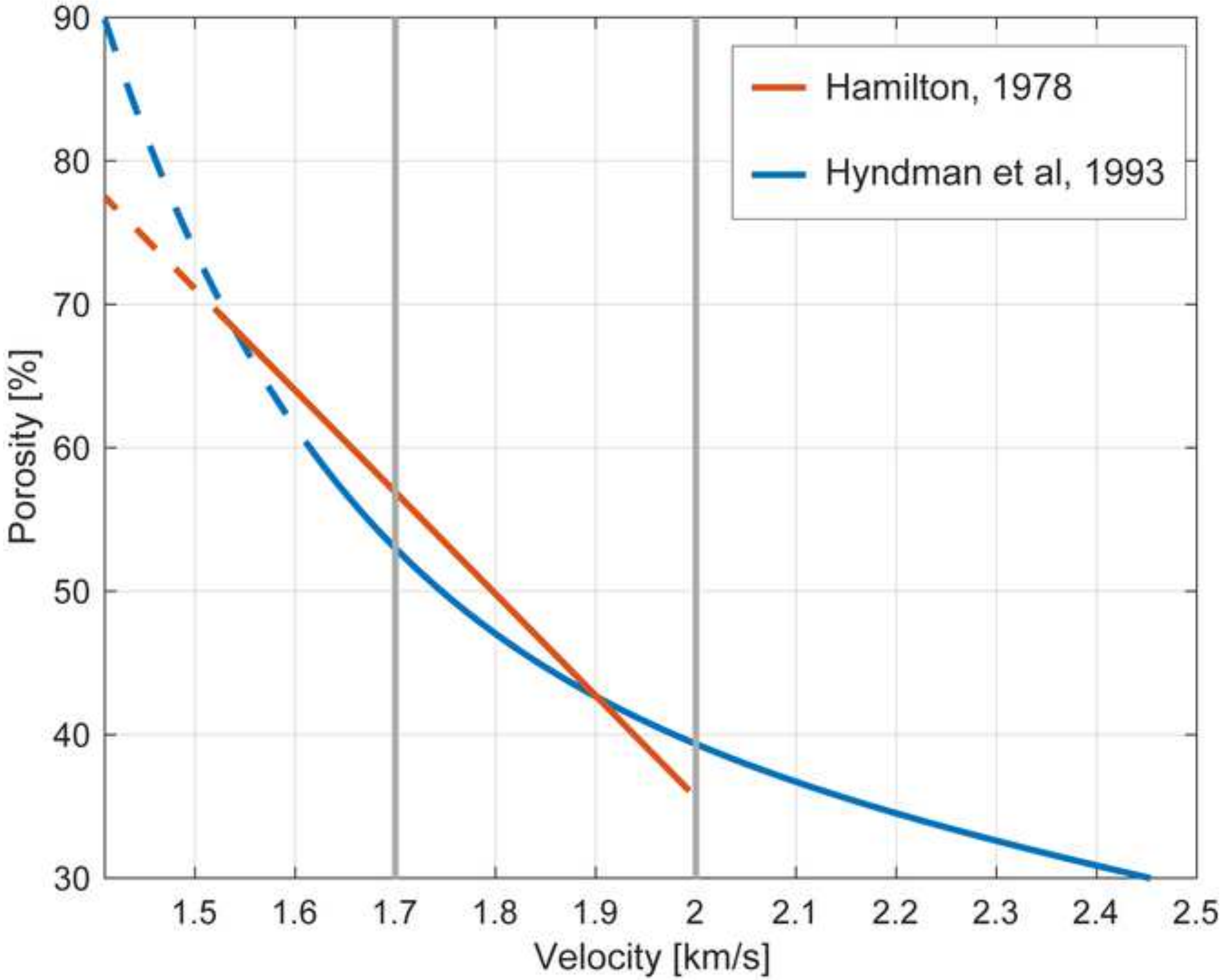

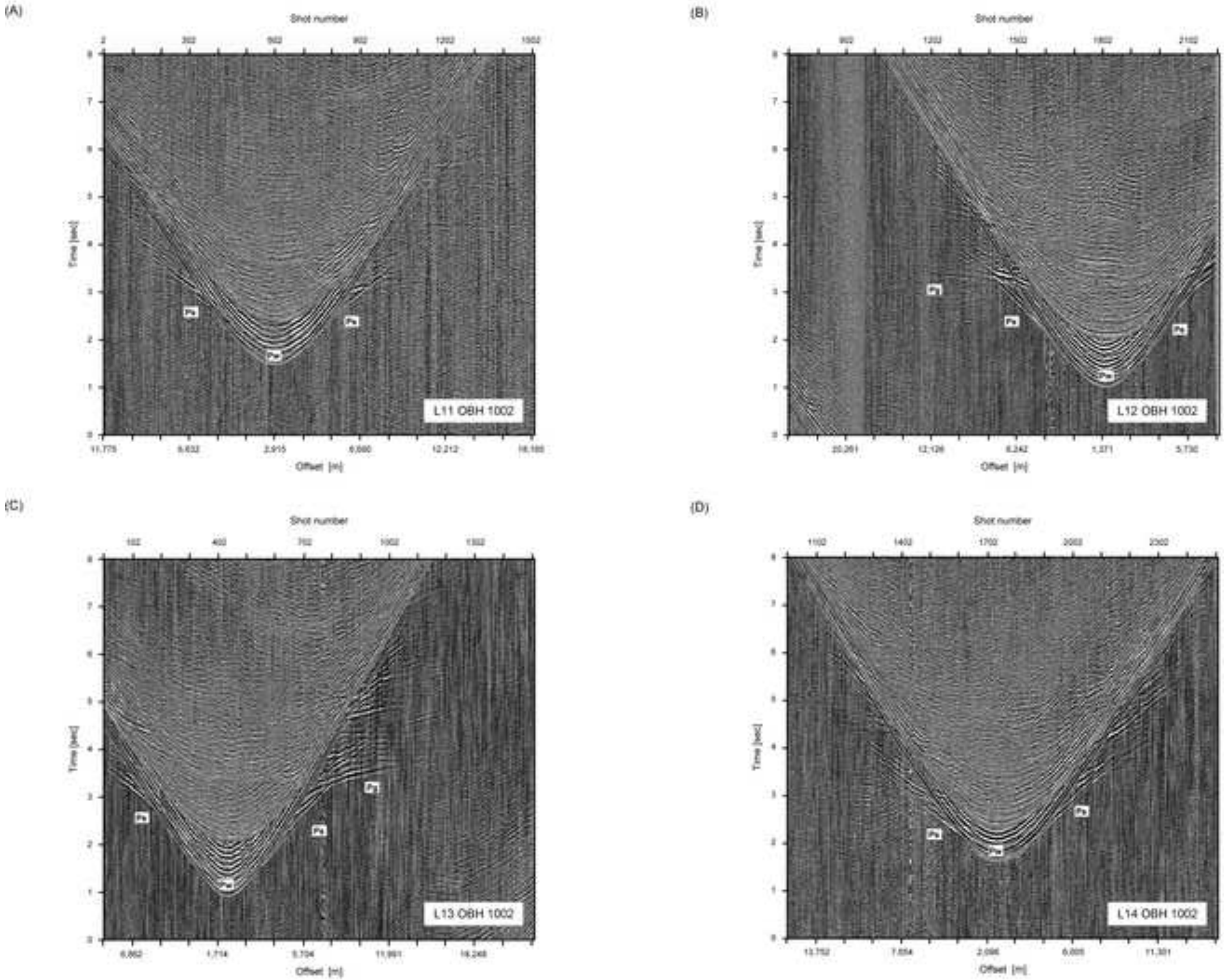
(A)
Shot number
Time [sec]
Offset [m]
L11 OBH 1002
(B)
Shot number
Time [sec]
Offset [m]
L12 OBH 1002
(C)
Shot number
Time [sec]
Offset [m]
L13 OBH 1002
(D)
Shot number
Time [sec]
Offset [m]
L14 OBH 1002

Declaration of interests

☒ The authors declare that they have no known competing financial interests or personal relationships that could have appeared to influence the work reported in this paper.

☐The authors declare the following financial interests/personal relationships which may be considered as potential competing interests:

Research Data

Click here to download Research Data https://osf.io/jdv54/